This is the peer-reviewed, final accepted version for American Mineralogist, published by the Mineralogical Society of America.
The published version is subject to change. Cite as Authors (Year) Title. American Mineralogist, in press.
DOI: https://doi.org/10.2138/am-2022-8336. http://www.minsocam.org/

Revision 3

Multi-stage metasomatic Zr mineralization in the world-class Baerzhe Rare-earth element-Nb-Zr-Be deposit, China

MINGQIAN WU[1,2,*], IAIN M. SAMSON[1], KUNFENG QIU[2,*], DEHUI ZHANG[2]

[1] School of the Environment, University of Windsor, Windsor, Ontario, Canada, N9B 3P4

[2] State Key Laboratory of Geological Processes and Mineral Resources, School of Earth Sciences and Resources, China University of Geosciences, Beijing 100083, China

* E-mail: aria.wu@uwindsor.ca; kunfengqiu@qq.com

ABSTRACT

Magmatic and metasomatic zircon occurs in many alkaline igneous rocks and both are potential economic reservoirs of Zr, and in some places, rare-earth elements. The Baerzhe deposit in China is an example of a system where both types of zircon occur. Previous studies recognized deuteric and variably altered magmatic zircon in a transsolvus miaskitic granite, as well as four types of metasomatic zircon in a transsolvus agpaitic granite. In this study, the relationships among, and origins of, zircon and how these relate to models for rare-metal mineralization are assessed. In-situ back-scattered electron (BSE) and cathodoluminescence (CL) imaging, Raman spectroscopy (including mapping), and chemistry of zircon from the agpaitic granite were conducted, combined with evaluation of published data on zircon from Baerzhe. Their textural, spectroscopic, and chemical characteristics suggest that the four types of metasomatic zircon in the agpaitic granite were not subjected to metamictization or intense alteration, with trace-element accommodation largely following a xenotime substitution mechanism. The most abundant type of metasomatic zircon in the agpaitic granite occurs in zircon-quartz pseudomorphs and exhibits comparable CL, Raman spectral, and chemical features to rare zircon

This is the peer-reviewed, final accepted version for American Mineralogist, published by the Mineralogical Society of America.
The published version is subject to change. Cite as Authors (Year) Title. American Mineralogist, in press.
DOI: https://doi.org/10.2138/am-2022-8336. http://www.minsocam.org/

that has partially replaced elpidite. This confirms that the pseudomorphs formed by complete replacement of elpidite. The pseudomorph zircon occurs in association with snowball quartz that contains inclusions of zircon, aegirine, and albite, and with secondary quartz containing aegirine. This is consistent with their coeval formation during Na metasomatism. The restriction of Na metasomatism to the agpaitic granite indicates that this event and the associated zircon formation resulted from early autometasomatism of the agpaitic phase. REE- and Be-rich zircon that replaced magmatic amphibole crystallized as a result of reaction with a REE- and Be-rich fluid that most likely was responsible for the later REE-Nb-Be mineralization that affected both the miaskitic and agpaitic granites. The miaskitic granite contains deuteric and altered magmatic zircon with different chemical characteristics to the four types of metasomatic zircon in the agpaitic granite. This suggests that secondary Zr mineralization in the miaskitic granite formed from different fluids to those that metasomatized the agpaitic granite and may also have resulted from autometasomatism. This study reveals a complex picture for the formation of zircon at Baerzhe, the character of which can vary significantly, both temporally and spatially. Such variable chemistry of the various types of zircon resulted not only from their different origins (magmatic vs. metasomatic), but also from localized water-rock interaction that involved multiple stages of fluids. Zircon in both the miaskitic and agpaitic phases was mainly the product of autometasomatism that was constrained to their parental granites.

INTRODUCTION

Metasomatic zircon is not abundant in common igneous rocks but is one of the most important ore minerals for Zr, and in some cases the rare-earth elements, in alkaline-peralkaline rare-metal-enriched systems (e.g., Kovalenko et al., 1995; Feng and Samson, 2015; Kynicky et al., 2011;

Marks and Markl, 2017; Möller and Williams-Jones, 2017; Wu et al., 2021). Previous studies (e.g., Hoskin, 2005; Pettke et al. 2005; Bell et al., 2019) have shown that the textural and chemical characteristics of metasomatic zircon from different localities can vary considerably. Where magmatic and metasomatic zircon occurs in the same rock, the metasomatic variety has been differentiated from the magmatic counterpart through morphological and chemical analyses. However, without proper documentation of the mineralogy and petrography of the host rocks, textural/chemical and isotopic features cannot be used for discrimination of magmatic and metasomatic zircon, since magmatic and metasomatic zircon can exhibit similarities in these features in both the same and different rocks (Rubin et al. 1989, 1993; Hoskin and Schaltegger, 2003; Hoskin, 2005; Pettke et al. 2005; Schaltegger et al. 2005; Schaltegger 2007; Wu et al., 2018; Qiu et al., 2019; Yang et al., 2013, 2014). Yet, little is known about how the chemistry of different generations of metasomatic zircon change through time during water-rock interaction in a given system. This study builds upon our current understanding of the granitic phases and mineralization in the large Baerzhe rare-earth element (REE)-Nb-Zr-Be deposit in Inner Mongolia, Northeast China, where different types of metasomatic zircon were identified in an agpaitic granite (Wu et al., 2021).

In this contribution, a variety of microbeam techniques are used to characterize the structural and chemical features of the different types of metasomatic zircon at Baerzhe in order to assess models for zircon formation and the fluid-rock interaction history of the deposit. In addition, we discuss previous textural, geochronological, and isotopic studies at Baerzhe in the context of the new data. We propose a refined multi-stage model for zircon formation and discuss the factors that may have controlled zircon chemistry during metasomatism. Differences in the chemistry of

This is the peer-reviewed, final accepted version for American Mineralogist, published by the Mineralogical Society of America.
The published version is subject to change. Cite as Authors (Year) Title. American Mineralogist, in press.
DOI: https://doi.org/10.2138/am-2022-8336. http://www.minsocam.org/

77 metasomatic zircon in different units of the miaskitic-agpaitic complex at Baerzhe, along with
78 the distribution of alteration, lead us to conclude that fluid-rock reactions during metasomatic
79 zircon formation largely involved autometasomatism.
80
81 **THE BAERZHE DEPOSIT**
82 The Baerzhe deposit, located in Inner Mongolia, Northeast China, at the eastern part of the
83 Central Asian orogenic belt (Fig. 1A), contains world-class endowments of rare-metal
84 mineralization hosted in an alkaline-peralkaline, multi-phase, granitic pluton (Fig. 1B). The
85 deposit contains approximately 1.0 Mt of total REE oxides (TREO) at an average grade of 0.57
86 wt % and 300 Kt of Nb_2O_5 at an average grade of 0.24 wt % (Fig. 2). In addition, ca. 2.8 Mt of
87 ZrO_2 at an average grade of 2.73 wt % and 48,470 t of BeO at an average grade of 0.05 wt % are
88 potential by-products from the extraction of REE and Nb (Qiu et al., 2019; Wu et al. 2021). The
89 Baerzhe deposit contains a large variety of rare-metal silicates, oxides, and carbonates, however,
90 most REE and almost all Be are hosted in hingganite ($(REE,Ca)_2(\square,Fe^{2+})Be_2[SiO_4]_2(OH)_2$), a
91 member of the gadolinite supergroup; zircon is the only ore mineral for Zr (Yang et al., 2020;
92 Wu et al., 2021).
93
94 The Baerzhe pluton, which was emplaced between ca. 127 and 123 Ma (zircon U-Pb ages from
95 Yang et al., 2013 and Qiu et al., 2019), intruded into Late Jurassic volcanic rocks (cf. Fig. 1C of
96 Wu et al., 2021). The pluton evolved from an unaltered hypersolvus miaskitic granite porphyry,
97 through a transsolvus miaskitic granite, to a transsolvus agpaitic granite (The definition of
98 agpaitic vs. miaskitic is after Marks and Markl, 2017; at Baerzhe, primary elpidite is present in
99 the agpaitic granite whereas the miaskitic granite contains zircon as the only primary Zr mineral)

This is the peer-reviewed, final accepted version for American Mineralogist, published by the Mineralogical Society of America.
The published version is subject to change. Cite as Authors (Year) Title. American Mineralogist, in press.
DOI: https://doi.org/10.2138/am-2022-8336. http://www.minsocam.org/

(Wu et al., 2021). Both of the transsolvus phases have been variably hematized but only the agpaitic granite was affected by ubiquitous Na metasomatism (Fig. 3). The presence of the altered agpaitic phase was only recently reported by Wu et al. (2021). REE-Nb-Be mineralization occurs in both the altered miaskitic and agpaitic granites, whereas high-grade Zr mineralization ($\geq$ 2.5 wt % of ZrO_2) is present only in the altered agpaitic granite (Wu et al., 2021). A minor, unmineralized, fine-grained hypersolvus granite (Fig. 3) was suggested to have crystallized from a different batch of melt that segregated and deviated from the main magmatic lineage at an early stage (Wu et al., 2021).

THE CURRENT MODEL OF MINERALIZATION

Five stages (a magmatic stage followed by four metasomatic stages) of rare-metal mineralization were identified at Baerzhe by Wu et al. (2021). Stage I is represented by the emplacement of the miaskitic and agpaitic granites. In addition to alkali feldspar and quartz, alkaline amphibole (arfvedsonite and fluoro-arfvedsonite) crystallized in both the miaskitic and agpaitic granites, whereas elpidite and possibly other alkaline zirconosilicates crystallized only in the agpaitic phase.

Stage II is characterized by Na metasomatism, zircon crystallization, and the formation of snowball quartz (poikilitic quartz crystals or aggregates that contain concentrically-zoned mineral inclusions; Figs. 4A, B) and by secondary quartz that contains randomly oriented aegirine inclusions and both zircon-quartz and REE-Nb-Be-rich pseudomorphs (Wu et al., 2021). These Stage II products are restricted to the agpaitic granite. Principal minerals in this stage are aegirine, albite, zircon, and quartz; minor minerals are astrophyllite, annite, hematite, and pyrite.

This is the peer-reviewed, final accepted version for American Mineralogist, published by the Mineralogical Society of America.
The published version is subject to change. Cite as Authors (Year) Title. American Mineralogist, in press.
DOI: https://doi.org/10.2138/am-2022-8336. http://www.minsocam.org/

Sodium metasomatism is represented by aegirine and albite, which replaced amphibole and K-feldspar, respectively. The most abundant type of zircon in these rocks occurs in zircon-quartz pseudomorphs (Fig. 4C), suggested by Wu et al. (2021) to have replaced elpidite. Zircon that replaced alkaline amphibole, mainly along with astrophyllite, annite, and minor hematite (Fig. 4D), is also abundant. These two replacement types account for the majority of the high-grade Zr mineralization at Baerzhe. The zircon-quartz pseudomorphs contain no protocryst relicts, however, a few examples of relict elpidite crystals that were replaced by zircon and calciocatapleiite (Fig. 4E) are preserved inside snowball quartz crystals. The latter type of zircon is referred to below as elpidite-replacement zircon. Finally, zircon occurs as inclusions in snowball quartz (inclusion zircon). This type does not contribute significantly to the overall Zr budget in the agpaitic rocks. Inclusion zircon crystals occur together with more abundant aegirine and albite inclusions in snowball quartz (Fig. 4B).

Wu et al. (2021) hypothesized that the various types of zircon and the snowball quartz formed in the same event and from the same fluid. The rationale for this was that (1) snowball quartz and all zircon types coexist and are in physical proximity in the agpaitic granite; (2) snowball quartz and quartz in the zircon-quartz pseudomorphs are in optical continuity and in some cases the pseudomorphs occur within snowball quartz crystals; and (3) commonplace replacement of the amphibole-replacement zircon by bastnäsite, which indicates that this zircon is relatively early in the evolution of the system as bastnäsite is a key mineral in a later event (Fig. 4D). The contemporaneity of snowball quartz formation and Na metasomatism (e.g., aegirine replacement of amphibole) is supported by the common presence of euhedral aegirine inclusions in snowball quartz. In summary, Wu et al. (2021) identified four types of metasomatic zircon in the agpaitic

This is the peer-reviewed, final accepted version for American Mineralogist, published by the Mineralogical Society of America.
The published version is subject to change. Cite as Authors (Year) Title. American Mineralogist, in press.
DOI: https://doi.org/10.2138/am-2022-8336. http://www.minsocam.org/

146 phase (i.e., inclusion, elpidite-replacement, pseudomorph, and amphibole-replacement) and
147 suggested that their formation is concomitant and constrained to Stage II.
148
149 The subsequent Stage-III event is the main stage of REE-Nb-Be ore formation, which affected
150 both the altered miaskitic and agpaitic granites. REE-Nb-Be mineralization occurs mainly
151 through complete pseudomorphism of unknown protocrysts (Fig. 4F) but also as partial
152 replacement of Stage II minerals (i.e., amphibole, aegirine, and zircon) (Wu et al., 2021). Major
153 minerals in Stage III are hingganite, hematite, ilmenite, columbite, aeschynite, and quartz. Stages
154 IV and V minerals replaced minerals of stages II and III, caused some further enrichment of
155 heavy REE (HREE) and Nb (crystallization of euxenite), and evolved into light REE (LREE =
156 La – Eu) enrichment, manifested by overprinting of LREE-dominant fluoro-carbonates and
157 fluorides on earlier minerals (Wu et al., 2021). Stages IV and V affected both the altered
158 miaskitic and agpaitic rocks. Additional details of the mineral assemblages and paragenesis can
159 be found in Wu et al. (2021).
160
161 **UNCERTAINTIES AND QUESTIONS WITH ZIRCON MINERALIZATION AT BAERZHE**
162 In the model of Wu et al. (2021), the four types of metasomatic zircon in the agpaitic phase were
163 suggested to have formed penecontemporaneously during Stage II. There are, however, a number
164 of reasons to question this interpretation. As the four types are never in physical contact, their
165 contemporaneity could not be demonstrated with textural evidence. Optical continuity, which
166 was used to suggest co-precipitation of snowball quartz and the zircon-quartz pseudomorphs,
167 could also have resulted from syntaxial overgrowth of snowball quartz on the quartz in the
168 pseudomorphs (cf. Goldstein and Rossi, 2002; Okamoto and Sekine, 2011; Michaud and

169 Pichavant, 2020). Only the amphibole-replacement zircon occurs with substantial amounts of
170 Fe^{2+} minerals (astrophyllite and annite), whereas the other types of zircon occur mainly in
171 association with Fe^{3+} minerals (aegirine and hematite). Finally, the possibility of different
172 generations of zircon is indicated by the variable chemistry and oxygen isotopic compositions of
173 zircon from Baerzhe as reported by Yang et al. (2013, 2014). Thus, the metasomatic zircon could
174 have different origins and have crystallized sequentially, rather than concomitantly.
175
176 Yang et al. (2013, 2014) identified magmatic and hydrothermal zircon in a hypersolvus,
177 unmineralized granite and a subsolvus, mineralized granite, respectively. The subsolvus
178 character of the latter, however, was not supported by any petrological description, and this
179 granite phase was not observed by Wu et al. (2021). However, in Yang et al. (2020), four photos
180 are provided (their Fig. 3) of what they interpreted as a subsolvus granite, which contains
181 euhedral perthite and microcline crystals, zircon-quartz pseudomorphs, and replacement of
182 amphibole by aegirine. These observations contradict the subsolvus interpretation of this unit and
183 suggest that it is the Na-metasomatized, agpaitic, transsolvus granite described by Wu et al.
184 (2021). It is not known, however, whether the hydrothermal zircon reported earlier by Yang et al.
185 (2013, 2014) was actually from the agpaitic transsolvus granite that was incorrectly described as
186 subsolvus by Yang et al. (2020), and is equivalent to one of the four types of metasomatic zircon
187 identified by Wu et al. (2021), or is from an unspecified subsolvus granite. In addition,
188 classification of these two types of zircon by Yang et al. (2013, 2014) was based on their zoning
189 characteristics in cathodoluminescence images and their REE patterns. Their magmatic zircon
190 exhibited oscillatory zoning, whereas their hydrothermal zircon was unzoned, and the two types
191 had chondrite-normalized REE patterns that corresponded to magmatic and hydrothermal zircon

This is the peer-reviewed, final accepted version for American Mineralogist, published by the Mineralogical Society of America.
The published version is subject to change. Cite as Authors (Year) Title. American Mineralogist, in press.
DOI: https://doi.org/10.2138/am-2022-8336. http://www.minsocam.org/

as defined by Hoskin (2005). Yang et al. (2014) also described a third type of zircon from the subsolvus, mineralized granite that was porous and exhibited heterogeneous zoning and which they ascribed to metamictization due to alteration and dissolution of magmatic zircon. However, the assignment of zircon origin was achieved through interpretation of the textural and chemical features of mineral separates, without documentation of the associated mineral assemblages and occurrences of zircon in the rocks. Although Yang et al. (2014, 2020) concluded that hydrothermal Zr and REE-Nb-Be mineralization both formed during a transitional, magmatic-hydrothermal period, they did not describe the relationship between Zr and REE-Nb-Be mineralization, nor the mineralogical characteristics of the host rocks. Furthermore, as mentioned in the Introduction, concluding that zircon types are magmatic or hydrothermal based on their REE patterns is unreliable at best and could lead to erroneous interpretations of zircon origin (Pettke et al., 2005; Bell et al., 2019). In the case of Baerzhe, this, in turn, could undermine one of the key conclusions of Yang et al. (2013), which is that meteoric water was involved in metasomatic zircon formation, an interpretation based on the O isotopic composition of what they interpreted as metasomatic zircon.

More recently, Qiu et al., (2019) documented magmatic and deuteric zircon in a mineralized transsolvus granite, samples of which were collected from 94 m to 119 m of the ZK7-02 drill core and at surface (cf. Wu et al., 2021). In SEM-CL images, magmatic zircon exhibits regular, bright oscillatory zoning and is in equilibrium with primary mineral assemblages, whereas deuteric zircon occurs as a partial replacement of amphibole, and displays irregular, dark oscillatory zoning. Samples that host the magmatic and deuteric zircon identified by Qiu et al. (2019) are from the hematized miaskitic granite described above, which lacks Na metasomatism

This is the peer-reviewed, final accepted version for American Mineralogist, published by the Mineralogical Society of America.
The published version is subject to change. Cite as Authors (Year) Title. American Mineralogist, in press.
DOI: https://doi.org/10.2138/am-2022-8336. http://www.minsocam.org/

215 but contains REE, Nb, and Be mineralization. The different rock types described above in this
216 section are summarized in Table 1.
217
218 The uncertainties described above call for a re-evaluation of the origin, timing, and chemistry of
219 different types of zircon at Baerzhe in the context of the revised geological and paragenetic
220 framework of Wu et al. (2021). Therefore, the first question to be investigated is whether all
221 zircon in the agpaitic rocks formed during a single stage from the same fluid, or in multiple
222 stages from more than one fluid. A second question is how the zircon separates reported by Yang
223 et al. (2013, 2014) relate to the detailed paragenesis and petrography of Wu et al. (2021). Testing
224 the latter question might reveal which rock phase(s) the hand-picked zircon crystals (or
225 fragments) examined by Yang et al. (2013, 2014) are from. To shed light on these questions,
226 chemical analyses were carried out on the four types of metasomatic zircon in the agpaitic
227 granite. Also in this rock phase, chemical analyses were conducted on the aegirine inclusions
228 hosted in snowball quartz and secondary quartz, the latter of which can host both zircon-quartz
229 and REE-Nb-Be-rich pseudomorphs (cf. Wu et al., 2021). In addition, Raman spectroscopy and
230 SEM-CL imaging were used to examine the structural state of the zircon. These results are
231 compared with previously published Raman, CL, and chemical data on zircon at Baerzhe.
232
233 ## ANALYTICAL METHODS
234 The optical characteristics of zircon were examined using an Olympus BX 51 polarizing
235 microscope. An SEM was used for back-scattered electron (BSE) imaging of zircon and aegirine.
236 Analyses were performed at the Centre for Advanced Microscopy and Materials
237 Characterization, University of Windsor, using an FEI Quanta 200 FEG environmental SEM. CL

imaging of zircon was carried out using the same SEM, coupled with a Centaurus cathodoluminescence detector. For both BSE and CL images, the instrument was operated in high vacuum mode, with a 20-kV accelerating voltage, a beam current of 30 nA, and a ca. 1.5-μm beam diameter.

Laser Raman spectroscopy was used for spot analyses and mapping of metasomatic zircon in the agpaitic granite, and was performed at the Centre for Advanced Microscopy and Materials Characterization, University of Windsor. A WITec Alpha 300 Raman spectrometer with a 532-nm air-cooled argon-ion laser was used as the excitation source. The output laser power was set to ~ 45 mW for spot analyses and ~ 30 mW for mapping. A ×50 or ×100 objective lens was used to focus the laser. Automated, tunable Raman filter maps, where higher brightness reflects higher intensity of a peak, were generated for the inclusion and pseudomorph zircon to assess variations in the structural state of the different CL domains in a single crystal.

Electron microprobe analyses (EMPA) were conducted at the Earth and Planetary Materials Analysis Laboratory, Western University, Canada, using a JEOL JXA-8530F microprobe. The operating conditions were a 15-kV accelerating voltage, a 20-nA beam current, a 5- or 10-μm beam diameter. For zircon, the standards used were pure metals (Zn, Nb, Hf, Th, and U), garnet (Y), rutile (Ti), diopside (Mg), augite (Al), zircon (Si, Zr), albite (Na), orthoclase (K), anorthite (Ca), apatite (P), rhodonite (Mn), and fayalite (Fe). For aegirine, augite (Si, Al), fayalite (Fe), diopside (Mg, Ca), rhodonite (Mn), albite (Na), orthoclase (K), rutile (Ti), zircon (Zr), and pure metals of Zn and Nb were used as standards. Peak counting times were 25 seconds and all data

This is the peer-reviewed, final accepted version for American Mineralogist, published by the Mineralogical Society of America.
The published version is subject to change. Cite as Authors (Year) Title. American Mineralogist, in press.
DOI: https://doi.org/10.2138/am-2022-8336. http://www.minsocam.org/

were corrected using the ZAF correction procedures. The full dataset for zircon and aegirine is provided in Appendices 1 and 2, respectively.

Laser-ablation inductively-coupled plasma mass spectrometry (LA-ICP-MS) analyses were undertaken using a PhotonMachines 193 nm short pulse width Analyte Excite excimer laser ablation system coupled with an Agilent 7900 fast-scanning quadrupole mass spectrometer, located at the Element and Heavy isotope analytical Laboratory at the University of Windsor. The energy, repetition rate, and raster rate were set at 2 mJ, 25 Hz, and 5 µm/s, respectively. A ca. 20-µm laser beam width was used for analyses of zircon and aegirine. The acquisition time was set at 50 seconds, including a 30-second acquisition for the gas background. Although precise replication of the spots used in EMPA in the LA-ICP-MS analyses was not possible because of the different approaches used in the two methods, laser ablation traverses were performed on the same crystals used for EMPA. The synthetic glass standard reference material (NIST 610) was used as the external calibration standard. Si concentrations from EMPA analyses were used as the internal standard. The following masses of Be, Si, Y, and lanthanides were measured for both zircon and aegirine, and the resulting average element detection limits are given in parts per million in parentheses: ^{9}Be (0.09), ^{29}Si (415), ^{89}Y (0.12), ^{139}La (0.06), ^{140}Ce (0.05), ^{141}Pr (0.01), ^{142}Nd (0.01), ^{152}Sm (0.02), ^{153}Eu(0.01), ^{158}Gd (0.01), ^{159}Tb (0.01), ^{164}Dy (0.02), ^{165}Ho (0.01), ^{166}Er (0.01), ^{169}Tm (0.01), ^{174}Yb (0.01), ^{175}Lu (0.02). Additional masses of ^{7}Li (0.61), ^{39}K (1.58), ^{44}Ca (1.13), ^{45}Sc (0.53), ^{50}Ti (1.73), ^{66}Zn (0.96), ^{93}Nb (0.10), ^{180}Hf (0.87), and ^{181}Ta (0.06) were analyzed only for zircon. The raw data were processed using the Iolite software, implemented upon the Igor Pro host environment (Paton et al., 2011). The full trace-element datasets for zircon and aegirine are provided in Appendices 1 and 2, respectively.

This is the peer-reviewed, final accepted version for American Mineralogist, published by the Mineralogical Society of America.
The published version is subject to change. Cite as Authors (Year) Title. American Mineralogist, in press.
DOI: https://doi.org/10.2138/am-2022-8336. http://www.minsocam.org/

Consistency of the results was checked using the concentrations of Ti, Nb, and Hf in zircon measured by both methods (LA-ICP-MS vs. EMPA) (cf. Appendix 3); all three elements show good correlations between the two methods, with R^2 values of 0.973, 0.913, and 0.920, respectively.

RESULTS

In general, the inclusion, pseudomorph, and elpidite-replacement zircon crystals exhibit no evidence of porosity, a feature that is commonly taken as evidence of later replacement, and have planar contacts with their co-precipitated minerals (i.e., aegirine, albite, and quartz) (Figs. 4B, C, E; 5; 6A, B). The amphibole-replacement zircon is, however, somewhat porous (Figs. 4D; 6C, D).

No compositional zoning is evident in BSE images of the four types of metasomatic zircon (Figs. 4B – E; 5B). Zoning is also generally not evident in optical images, but some inclusion zircon crystals contain irregular areas that are darker brown than the rest of the crystals (Fig. 5A). All of the examined metasomatic zircon, however, shows zoning in CL images. Two or three CL domains are present in the inclusion zircon. Domain I is the dark brown areas of the inclusion zircon that are present only in some crystals (Fig. 5A). This domain exhibits dull, unzoned CL, or irregular, chaotic luminescence with weak oscillatory zoning (Fig. 5C). Domain II occurs as a mantle to Domain I, where present, but otherwise constitutes the centre of most crystals, and is overall somewhat darker than a surrounding rim (Domain III) (Fig. 5C). Both domains II and III exhibit the same type of oscillatory zoning (Fig. 5C). The pseudomorph and elpidite-replacement zircon generally display more irregular zoning than the inclusion zircon, but have comparable

This is the peer-reviewed, final accepted version for American Mineralogist, published by the Mineralogical Society of America.
The published version is subject to change. Cite as Authors (Year) Title. American Mineralogist, in press.
DOI: https://doi.org/10.2138/am-2022-8336. http://www.minsocam.org/

306 CL characteristics to one another, with three irregularly-shaped domains with different levels of
307 luminescence (Figs. 5D – G; 6B). Domain I is dull, unzoned or weakly zoned, and mostly
308 constitutes the core of a pseudomorph or elpidite-replacement zircon crystal (Figs. 5E, G; 6B).
309 Domain II is brighter than Domain I, and occurs as unzoned or weakly-zoned mantles
310 surrounding Domain I (Figs. 5E, G; 6B). Domain III exhibits the brightest CL and occurs as
311 sporadic, elongated patches within both domains I and II (Figs. 5E, G; 6B). In contrast to the
312 internal zoning shown by the other types of zircon, the amphibole-replacement zircon is
313 homogeneous, with no zoning, and very dull CL (Figs. 6C, D).
314
315 **Raman spectroscopy**
316 The four types of metasomatic zircon yield similar Raman spectra, with five distinct Raman
317 bands at 206 – 212, 349 – 356, 436 – 440, 969 – 975, and 1,000 – 1,008 cm^{-1} (Appendix 4). The
318 wavenumbers and relative peak intensities of these spectra match those of non-metamict zircon
319 reported elsewhere (e.g., Nasdala et al., 1995, 2001; Zhang et al., 2000). The amphibole-
320 replacement, elpidite-replacement, and pseudomorph zircon crystals yielded comparable and
321 intense ν_3 (SiO_4) Raman bands that range from 1,003 to 1,008 cm^{-1}, and that have FWHM (full
322 width at half-maximum) values that are close to 5 cm^{-1} (Appendices 4; 5). The inclusion type
323 zircon exhibits slightly lower ν_3 Raman bands (1,000 to 1,001 cm^{-1}), and overall marginally
324 wider FWHM values (5 – 6 cm^{-1}) (Appendices 4; 5).
325
326 The various domains shown in the CL images are also evident in the automated Raman filter
327 maps. Figures 7A – C are representative maps for an inclusion zircon crystal tuned to the 353 ± 5
328 cm^{-1}, 438 ± 5 cm^{-1}, and 1,001 ± 5 cm^{-1} peaks. The mantle-rim feature of the inclusion zircon

(Domains II and III) shown in CL images is not seen in the filter maps; rather, these two domains are characterized by comparable and heterogeneous brightness on the Raman maps. The dark brown area (Domain I) seen under optical imaging is mostly represented by the darkest part in a given inclusion crystal in the filter maps (Fig. 7A – C). In some cases, Domain I is characterized by lower intensities of only the 353 ± 5 cm^{-1} and 438 ± 5 cm^{-1} bands (darker on maps tuned to these two bands), but comparable intensities of the 1001 ± 5 cm^{-1} band (similar brightness on Raman maps to other domains).

Domains I and II in the pseudomorph zircon, are comparable in brightness on maps tuned to the 353 ± 5, 438 ± 5, and 1001 ± 5 cm^{-1} Raman bands (Figs. 7D – F). Domain III of the pseudomorph zircon differs from domains I and II in that the 353 ± 5 and 438 ± 5 cm^{-1} bands in Domain III are characterized by higher intensities (brighter on maps) (Figs. 7D, E) and the 1,001 ± 5 band by lower intensities (Fig. 7F).

Zircon chemistry

Three of the four types of zircon, namely the inclusion, elpidite-replacement, and pseudomorph, contain comparable ZrO_2, SiO_2, and ΣREE concentrations (Figs. 8A, B). All four types contain comparable and variable HfO_2 concentrations that range from 0.40 to 1.86 wt % (Fig. 8A), and all are enriched in HREE relative to LREE, with distinct negative Eu anomalies (Fig. 8C). Most metasomatic zircon contains <0.8 wt % UO_2 and <0.5 wt % ThO_2, with the inclusion zircon containing consistently low concentrations of both U and Th (Appendix 6A). Three amphibole-replacement zircon crystals are characterized by higher ThO_2 or UO_2 concentrations than the rest, and are plotted as outliers (Appendix 6A). The inclusion zircon differs from the other types in

This is the peer-reviewed, final accepted version for American Mineralogist, published by the Mineralogical Society of America.
The published version is subject to change. Cite as Authors (Year) Title. American Mineralogist, in press.
DOI: https://doi.org/10.2138/am-2022-8336. http://www.minsocam.org/

having positive slopes from La to Sm ($La_N/Sm_N < 1$) on chondrite-normalized plots (the other types have negative slopes; $La_N/Sm_N > 1$), a much steeper increase in concentrations from Gd to Lu than the other types (much lower Gd_N/Yb_N values), and positive Ce anomalies (the other types have no Ce anomaly) (Fig. 8C). In addition, the inclusion zircon generally contains higher concentrations of Na, K, Fe, Zn, and Ti, and higher Ta/Nb values than the other types (Appendices 6).

The major- and trace-element chemistry of elpidite-replacement and pseudomorph zircon largely overlaps such that they together comprise a single population (Fig. 8; Appendices 6; 7). These two types generally exhibit the highest La/Yb values of the four zircon types and have relatively flat chondrite normalized REE patterns and concave-down HREE patterns. Although LREE concentrations of the elpidite-replacement and pseudomorph zircon are more than an order of magnitude higher than the inclusion zircon, the ΣREE concentrations of these three types are comparable and range from ca. 0.4 wt % to 1.3 wt %. The amphibole-replacement zircon exhibits REE patterns that are similar to those of the elpidite-replacement and pseudomorph zircon, but several times to an order of magnitude higher LREE and HREE concentrations than the other types, with approximately 3 to 6 wt % ΣREE (Fig. 8C; Appendix 7). In addition, the amphibole-replacement zircon is characterized by Be concentrations (ca. 200 ppm) that are more than four times higher than the other three types of zircon (Appendix 6). Note that the trace-element chemistry of the different domains identified within individual crystals of the inclusion and pseudomorph zircon using CL and Raman spectroscopy could not be characterized given the spatial resolution possible with LA-ICP-MS. Thus, the trace-element analyses of these zircon crystals represent a mixture of all three domains.

This is the peer-reviewed, final accepted version for American Mineralogist, published by the Mineralogical Society of America.
The published version is subject to change. Cite as Authors (Year) Title. American Mineralogist, in press.
DOI: https://doi.org/10.2138/am-2022-8336. http://www.minsocam.org/

375

376 **Aegirine inclusion chemistry**

377 Using the International Mineralogical Association (IMA) nomenclature for clinopyroxene of
378 Morimoto et al. (1988), the inclusions in snowball and secondary quartz from the agpaitic granite
379 at Baerzhe are sodic, with comparable, almost end-member, aegirine compositions: $Aeg_{88-93}Quad_{6-10}Jd_{1-5}$ (Appendix 8). Their ΣREE values are also similar (ca. 1,200 ppm) and they are
381 always LREE-rich with distinct negative Eu anomalies and weak negative Ce anomalies. Their
382 average LREE and HREE concentrations are 983 ppm and 189 ppm, respectively. As the
383 inclusion zircon that is associated with the aegirine inclusions in snowball quartz yielded
384 generally positive slopes from La to Lu with weak positive Ce anomalies, the chondrite-
385 normalized REE patterns of the aegirine inclusions are the opposite of the zircon inclusions,
386 except that they both show negative Eu anomalies (Fig. 8C).

387

388 **DISCUSSION**

389 **Were the zircon-quartz pseudomorphs originally elpidite?**

390 Wu et al. (2021) argued that the elpidite-replacement and pseudomorph zircon share the same
391 origin, and that the latter represents complete replacement of elpidite. This interpretation,
392 however, was not rigorously tested in Wu et al. (2021). The data presented above support this, as
393 the elpidite-replacement and pseudomorph have comparable CL, Raman, and major-/trace-
394 element chemical features. Our data further validate the interpretation that the Na-
395 metasomatized, transsolvus granite was agpaitic and crystallized magmatic Na zirconosilicates.
396 Therefore, in what follows, the term "pseudomorph zircon" will be used to represent both the
397 pseudomorph and the elpidite-replacement zircon, unless indicated otherwise. The formation of

This is the peer-reviewed, final accepted version for American Mineralogist, published by the Mineralogical Society of America.
The published version is subject to change. Cite as Authors (Year) Title. American Mineralogist, in press.
DOI: https://doi.org/10.2138/am-2022-8336. http://www.minsocam.org/

zircon-quartz pseudomorphs as a result of the replacement of primary Na zirconosilicates is also a common feature seen in the agpaitic phases at the Strange Lake and Khan Bogd REE-Nb-Zr-mineralized, miaskitic-agpaitic granitic complexes (Kynicky et al., 2011; Gysi and Williams-Jones, 2013), which share mineralogical and chemical similarities with Baerzhe (Wu et al., 2021). This indicates that the presence of zircon-quartz pseudomorphs could be a key characteristic of metasomatic Zr mineralization in agpaitic granites.

Post-crystallization modification of zircon

Raman spectroscopy is a useful method in the quantification of radiation damage (metamictization) in zircon (e.g., Nasdala et al., 1995). Generally, Raman spectra of well-ordered, non-metamict zircon are characterized by a v_3 band at about 1,007 cm^{-1} that has FWHM values of ca. 5 cm^{-1}. Variably disordered, metamict zircon, on the other hand, exhibits lower v_3 values (955 – 1,000 cm^{-1}) and higher FWHM values that range from 10 to 30 cm^{-1} (Appendix 5A) (Nasdala et al. 2001; Resentini et al., 2020). Thus, the four types of metasomatic zircon from Baerzhe are all well-ordered crystals, as their v_3 peaks lie between 1,000 and 1,008 cm^{-1} and have FWHM values close to 5 cm^{-1} (Appendix 5B).

A domain of zircon crystal that has experienced post-crystallization alteration normally shows different and irregular Raman, CL, or chemical features relative to a pristine, unaltered domain (e.g., Nasdala et al., 1995, 2001). Because Domain I in the inclusion zircon was overgrown by domains II and III, which both show oscillatory zoning, and shows textural equilibrium with aegirine (Figs. 5A – C), it most likely represents the earliest generation of inclusion zircon crystal growth. Some of the Domain I parts of inclusion zircon exhibit chaotic luminescence

421 under CL imaging (cf. Fig. 5C). Such CL characteristics could have resulted from post-
422 crystallization alteration, likely by the fluid that precipitated domains II and III. Likewise,
423 Domain III in pseudomorph zircon occurs as irregular patches within crystals, but never as
424 individual crystals. These observations suggest that Domain III in pseudomorph zircon
425 represents post-crystallization alteration of pre-existing zircon. As the inclusion and
426 pseudomorph zircon crystals are generally not porous and exhibit consistent compositions (cf.
427 Figs. 4 – 6; 8; Appendices 6; 7), these two types were not modified significantly. The minor
428 alteration of the inclusion and pseudomorph zircon added no additional Zr to the system, and
429 does not represent a separate Zr-forming event. Although the amphibole-replacement zircon was
430 partially replaced by bastnäsite, this event does not appear to have modified the chemistry or
431 structure of this zircon, as the BSE, CL, Raman, and chemical features of different amphibole-
432 replacement zircon crystals are invariably similar. Therefore, based on the generally comparable
433 BSE, CL, Raman, and chemical features of different crystals of each type from the four types of
434 metasomatic zircon, none was largely affected by post-crystallization modification.
435
436 What remains to be assessed is whether the slightly lower v_3 peaks and wider FWHM values of
437 the inclusion zircon represent minor metamictization. The fact that the inclusion zircon contains
438 the overall lowest U and Th concentrations of the various types of zircon (Appendix 6A)
439 suggests that the lower v_3 peaks and higher FWHM values in this type are not related to
440 metamictization, but more likely to the presence of substituting elements that distorted the zircon
441 structure. The inclusion zircon contains higher K, Ti, Zn, and Fe, and generally higher Na
442 concentrations than the other types (cf. Appendix 6). Greater substitution of Zr and Si by these
443 elements might cause more lattice modification, which could result in the slightly different

444 Raman spectral characteristics. The current data, however, do not allow us to test exactly which
445 elements are responsible.
446
447 Yang et al. (2014) reported rare, metamict zircon at Baerzhe. This is a misinterpretation, as this
448 "metamict" zircon is characterized by v_3 peaks between 1,004 and 1,005 cm^{-1}, with FWHM
449 values of 9 – 12 cm^{-1} (Yang et al. 2014). These values are close to the well-ordered zircon seen
450 in this study, and are different to metamict zircon (cf. Nasdala et al. 2001; Resentini et al., 2020).
451 Based on the presence of "dissolution pores" and irregular compositional zoning in these
452 "metamict" zircon grains (Yang et al., 2014), we suggest that these crystals have experienced
453 metasomatism but not metamictization (cf. Putnis, 2002). These crystals have comparable REE
454 characteristics with the inclusion zircon reported in this study, but contain higher Hf and P
455 concentrations (Appendix 9), which indicates that they are not the same as the inclusion zircon.
456
457 **Zircon compositions and fluid chemistry**
458 The data discussed above demonstrate that the metasomatic zircon in the agpaitic granite was not
459 subjected to metamictization or intense alteration, such that they will largely have retained their
460 original chemistry. The question is whether such zircon mineral compositions can be used to
461 infer the chemistry of the fluid from which they crystallized. To address this question, one needs
462 to first assess what the crystal chemical controls were. Also, whether zircon chemistry reflects
463 the parental fluid chemistry or what was being replaced (i.e., chemistry of the protocrysts) needs
464 to be taken into consideration.
465

466 The a.p.f.u. sum of the trivalent and pentavalent cations (ΣREE + Sc + Al + Fe^{3+} + Nb + Ta + P)
467 exhibits a coherent negative correlation with the a.p.f.u. sum of tetravalent cations (Si + Zr + Hf),
468 with a slope close to -1 (-0.84 for the pseudomorph zircon, -0.93 for the inclusion zircon, and -
469 0.97 for the amphibole-replacement zircon), and an overall R^2 of 0.98 (Fig. 9A). The analyzed
470 zircon crystals are, therefore, broadly consistent with a xenotime substitution (i.e., (ΣREE, Sc,
471 Al, Fe)$^{3+}$ + (Nb, Ta, P)$^{5+}$ = (Zr, Hf)$^{4+}$ + Si^{4+}) (cf. Hanchar et al., 2001; Yang et al., 2016). Figure
472 9A assumes that Fe is present entirely as Fe^{3+}. However, Fe could be present as Fe^{2+}, but would
473 require different, but theoretically feasible, substitution mechanisms (cf. Hanchar et al., 2001). If
474 Fe is removed from the xenotime model (if it is Fe^{2+}) (Fig. 9B), the correlation for inclusion
475 zircon, which contains significantly more Fe than the other types, is poorer and the slope (-0.48)
476 for the other elements (i.e., ΣREE + Sc + Al + Nb + Ta + P), is less consistent with the xenotime
477 model. This is also true to a lesser extent of the pseudomorph zircon. This suggests that Fe,
478 especially in the inclusion zircon, is present as Fe^{3+} and is consistent with the association of
479 inclusion aegirine, in which Fe is trivalent, and with the positive Ce anomalies seen in this
480 zircon. Fe is less important in the amphibole-replacement zircon and the xenotime model is not
481 affected if Fe is removed (Fig. 9A vs. 9B). This may suggest that Fe is present as Fe^{2+}, consistent
482 with the association of this type of zircon with astrophyllite and annite.
483
484 In summary, the data presented and discussed above enable us to conclude that the well-ordered
485 and unaltered metasomatic zircon at Baerzhe accommodated trace elements, including REE,
486 according to crystal chemical principles (dominated by the xenotime substitution). Thus, zircon
487 chemistry should be a reliable indicator of parental fluid chemistry, assuming that fluid-rock

This is the peer-reviewed, final accepted version for American Mineralogist, published by the Mineralogical Society of America.
The published version is subject to change. Cite as Authors (Year) Title. American Mineralogist, in press.
DOI: https://doi.org/10.2138/am-2022-8336. http://www.minsocam.org/

ratios were high and that zircon chemistry was not significantly influenced by the chemistry of precursor phases (which is discussed below).

Single- vs. multi-stage zircon formation in the agpaitic granite

Wu et al. (2021) argued that all metasomatic zircon from the agpaitic granite formed from the same fluid. In this hypothesis, one would predict that the investigated zircon all exhibits comparable trace-element chemistry, under conditions such that the chemistry of the various types of zircon was governed by parental fluid chemistry. The inclusion, pseudomorph, and amphibole-replacement, however, exhibit quite different trace-element chemistry (Fig. 8; Appendices 6; 7). The question is whether or not the composition of one or more varieties was governed by parental fluid chemistry and/or multiple fluids were involved in zircon formation.

If chemistry of the amphibole-replacement zircon was influenced by the protocryst (amphibole). one should expect that the amphibole-replacement zircon would in some way reflect amphibole chemistry. However, the high ΣREE (approximately 3 to 6 wt %) and Be (∽200 ppm) concentrations in the amphibole-replacement zircon (Fig. 8; Appendix 6D) cannot reflect inheritance from amphibole, as the replaced amphibole contains < 10, < 100, and <18 ppm of LREE, HREE, and Be, respectively (Wu et al., 2021). The amphibole-replacement zircon, therefore, precipitated from a REE- and Be-rich fluid, from which the amphibole-replacement zircon could efficiently sequester these elements.

As the inclusion zircon occurs exclusively inside snowball quartz, and exhibits equilibrium contacts with the inclusion aegirine, it precipitated directly from the fluid that caused the

This is the peer-reviewed, final accepted version for American Mineralogist, published by the Mineralogical Society of America.
The published version is subject to change. Cite as Authors (Year) Title. American Mineralogist, in press.
DOI: https://doi.org/10.2138/am-2022-8336. http://www.minsocam.org/

511 formation of metasomatic snowball quartz and that was responsible for Na metasomatism (cf.
512 Wu et al., 2021). This metasomatic origin for snowball quartz is further supported by the same
513 chemistry of aegirine inclusions in snowball and secondary quartz (Fig. 8C; Appendix 8).
514 Therefore, the chemistry of the inclusion zircon was governed by a fluid. The question arises as
515 to whether this fluid was the REE-Be-rich fluid from which the amphibole-replacement zircon
516 crystallized. If so, one should expect that the inclusion zircon would also contain high Be and
517 REE concentrations, which is not the case. Most importantly, the inclusion zircon not only
518 contains much lower Be (16 – 59 ppm) and ΣREE (0.5 ppm – 1.3 wt %) than the amphibole-
519 replacement zircon (∽200 ppm Be and 3 to 6 wt % ΣREE) but has higher concentrations of Na,
520 Fe, Zn, and Ta (cf. Fig. 8; Appendix 6). The possibility that the inclusion and amphibole-
521 replacement varieties are related through the addition or removal of REE and Be in a fluid during
522 water-rock interaction has to be considered; i.e., the two varieties crystallized from the same, but
523 evolving fluid. This scenario would require the crystallization or break-down of REE-Be
524 minerals (i.e., hingganite). However, the formation and replacement of hingganite postdated
525 zircon formation at Baerzhe, such that there is no viable source or sink for these elements in the
526 minerals present during zircon formation. Furthermore, amphibole-replacement and inclusion
527 zircon with the chemical characteristics described above occur in the same rock, such that
528 chemical evolution of a single fluid temporally or spatially, as would be required, would not
529 have been possible. Therefore, the data are most consistent with a model in which the inclusion
530 and amphibole-replacement zircon crystallized from two different fluids.
531
532 The high REE and Be concentrations in the amphibole-replacement zircon provide a link to the
533 REE-Nb-Be mineralization (Stage III) that postdated the Zr mineralization of Stage II. Therefore,

534 it is likely that the amphibole-replacement zircon formed from the Stage III fluid. This is
535 consistent with the textural observation that amphibole-replacement zircon always occurs outside
536 snowball quartz, which hosts all of the inclusion and some pseudomorph zircon (Wu et al.,
537 2021).
538
539 There is good textural evidence that the inclusion and pseudomorph varieties were coeval and
540 formed during Na metasomatism (Wu et al., 2021). Therefore, the most likely reason for the
541 differences in the chemistry of the inclusion and pseudomorph zircon is that the chemistry of the
542 pseudomorph zircon was influenced by inheritance from the protocryst (elpidite), rather than
543 reflective of the metasomatic fluid. This scenario, however, cannot be rigorously tested as it
544 would require trace-element chemistry of unaltered elpidite. As Na metasomatism is constrained
545 to the agpaitic granite, with strong evidence that this fluid also caused the precipitation of
546 snowball quartz and pseudomorph/inclusion zircon (i.e., Stage II), this event is interpreted to
547 represent autometasomatism and that the fluid did not infiltrate the miaskitic granites.
548
549 In summary, the discussion above supports a revised model in which the Stage II inclusion and
550 pseudomorph zircon crystallized from the same fluid during autometasomatism, followed by
551 amphibole-replacement zircon that crystallized from a later, Stage-III REE-Be-rich fluid.
552
553 **REE chemistry of inclusion zircon**
554 The REE chemistry of the inclusion zircon is distinct from the other types in that it has
555 significant LREE depletion and a positive slope on chondrite-normalized plots, as well as a
556 positive Ce anomaly (Fig. 8C). Such REE distributions of the inclusion zircon, which is

metasomatic in origin, though similar to magmatic zircon seen in most granitic settings (e.g., Hoskin and Schaltegger, 2003; Hoskin, 2005), is analogous to hydrothermal zircon from the Yankee Lode in the Mole granite, Australia (Pettke et al., 2005). The aegirine inclusions that co-precipitated with the inclusion zircon contain significantly higher LREE and lower HREE concentrations, and have complementary REE-normalized patterns to the inclusion zircon (Fig. 8). These two minerals are the only minerals in this assemblage that contain significant REE, given that the co-precipitated albite and quartz contain negligible amounts of REE (cf. Bea, 1996). Thus, the depletion in LREE plus Gd and Tb seen in the inclusion zircon, likely reflects the incorporation of the lighter REE into the co-precipitated aegirine, especially given the volumetric dominance of aegirine relative to zircon (cf. Wu et al., 2021). In an analogous manner, positive Ce anomalies in zircon and negative anomalies in aegirine likely reflect the partitioning of Ce^{4+} more readily into zircon than aegirine given that it has the same valence as Zr^{4+}, whereas the trivalent Fe site in aegirine better accommodates Ce^{3+} than Ce^{4+}.

Implications for the published petrological, isotopic, and geochronological data

The zircon-quartz pseudomorphs shown in Figure 3D of Yang et al. (2020) were equated by those authors to the hydrothermal zircon of Yang et al. (2013, 2014, 2020), in which only zircon mineral separates were analyzed. If that is the case, their hydrothermal zircon would be the same as the pseudomorph zircon described in Wu et al. (2021) and this study, although without petrographic context for the mineral separates, there is still some uncertainty. The fact that their hydrothermal zircon exhibits generally comparable REE chemical features to the pseudomorph zircon described here (Fig. 10), could add credence to this conclusion. However, there are several discrepancies between our descriptions of the pseudomorph zircon and the hydrothermal

580 zircon described by Yang et al. (2013, 2014, 2020). First, the hydrothermal zircon mineral
581 separates of Yang et al. (2013, 2014, 2020) mainly exhibit featureless CL, whereas the CL
582 images of zircon pseudomorphs reported here mostly exhibit a core-rim structure, although
583 Domain I can be occasionally featureless (Figs. 5E, G; 6B). Secondly, when the chemical data of
584 Yang et al. (2013, 2014, 2020) are combined with our data on the pseudomorph zircon, two
585 populations are evident in a bivariate plot of ZrO_2 vs. HfO_2 (Fig. 11). Population I consists of
586 probe data from this study, defining a trend that is characterized by invariably high
587 concentrations of ZrO_2 that decrease slightly with increasing HfO_2 concentrations. The probe
588 data of Yang et al. (2013, 2014) are also consistent with this trend. Population II represents the
589 probe data from Yang et al. (2020) that are characterized by variable ZrO_2 but invariably low
590 HfO_2 concentrations. There are two possible explanations for such differences. The first is that
591 the zircon pseudomorphs described by Wu et al. (2021) and this study are equivalent to the
592 hydrothermal zircon described in Yang et al. (2013, 2014, 2020), and this type of zircon can
593 exhibit different major-element chemistry and CL features, albeit with generally comparable
594 REE features. In this scenario, the subsolvus granite described in Yang et al. (2013, 2014, 2020)
595 is in fact the Na-metasomatized, agpaitic, transsolvus granite of Wu et al. (2021), which is
596 consistent with the presence of perthite and microcline in the same rocks (cf. Yang et al., 2020).
597 The differences in major-element chemistry could be explained if the two pseudomorph zircon
598 populations on Figure 11 represent replacement of two different alkali zirconosilicate protocrysts
599 that contained different Zr and Hf concentrations but had comparable REE characteristics that
600 were later inherited by the pseudomorph zircon. The alternative is that the hydrothermal zircon
601 reported by Yang et al. (2013, 2014), which follows the same trend as the pseudomorph zircon of
602 Population I, represents crystals from the zircon-quartz pseudomorphs, but that Population II

This is the peer-reviewed, final accepted version for American Mineralogist, published by the Mineralogical Society of America.
The published version is subject to change. Cite as Authors (Year) Title. American Mineralogist, in press.
DOI: https://doi.org/10.2138/am-2022-8336. http://www.minsocam.org/

603 from Yang et al. (2020) comprises zircon mineral separates from other rock types (possibly the
604 miaskitic phases), but were misinterpreted as the pseudomorph zircon. In either scenario, the
605 hydrothermal zircon reported by Yang et al. (2013, 2014) equates to the pseudomorph zircon
606 reported in Wu et al. (2021) and this study.
607
608 Yang et al. (2013, 2014) reported extremely low $\delta^{18}O$ values for the hydrothermal zircon
609 (pseudomorph zircon), and suggested that meteoric water entered the Baerzhe zircon-forming
610 system. If their interpretation is correct, the discussion above means that the incursion of
611 meteoric water occurred during zircon-quartz pseudomorph formation during autometasomatism
612 of the agpaitic granite. Autometasomatism, however, excludes participation of external fluids,
613 which is inconsistent with mixing of magmatic fluids with meteoric fluids during the formation
614 of pseudomorph zircon, as suggested by Yang et al. (2013, 2014). Given the uncertainties with
615 what was analyzed in the O-isotopic study, and how that relates to what has been documented in
616 this study, this contradiction will need to be addressed in future studies.
617
618 The deuteric and variably altered magmatic zircon in the hematized miaskitic granite reported by
619 Qiu et al. (2019) has different petrographic, textural, and chemical (cf. Fig. 12) characteristics to
620 the metasomatic zircon in the agpaitic granite reported here and by Wu et al. (2021). In addition,
621 the deuteric zircon of Qiu et al. (2019) has distinct chemistry relative to all the other reported
622 zircon compositions at Baerzhe (Yang et al., 2013, 2014, 2020; this study). These facts add more
623 credence to the fact that the inclusion and pseudomorph zircon from the agpaitic phases resulted
624 from autometasomatism. Moreover, in consideration of the interpretation that deuteric zircon,
625 which veins primary amphibole, was directly precipitated from a fluid (Qiu et al., 2019), the

626 fluid responsible for zircon mineralization and alteration in the transsolvus miaskitic granite was
627 constrained to that granite (possibly through autometasomatism), and was not one of the zircon-
628 forming fluids that affected the agpaitic granite.
629
630 Therefore, crystallization of metasomatic zircon at Baerzhe was governed by at least two stages
631 of autometasomatism that occurred in the transsolvus miaskitic and agpaitic granites. Abundant
632 REE- and Be-rich, amphibole-replacement zircon, which was suggested above to have formed
633 through reactions of later REE-Nb-Be-mineralizing fluid reacting with the agpaitic granite, was
634 hypothesized to have crystallized later than the other types of metasomatic zircon in the agpaitic
635 granite. This REE-Nb-Be-mineralizing fluid, unlike the Na metasomatism of the agpaitic granite
636 or the fluid responsible for deuteric zircon in the miaskitic granite, permeated both the
637 transsolvus agpaitic and miaskitic phases, and was responsible for ubiquitous hematization on
638 the transsolvus rocks (cf. Wu et al., 2021). In this case, one may predict that this REE-Nb-Be-
639 mineralizing fluid has precipitated some zircon in the altered miaskitic phase. This prediction can
640 be tested only if the Be concentration from the zircon from the altered miaskitic granite is
641 known. Two stages of autometasomatism, in combination with a more widespread REE-Nb-Be-
642 rich fluid contributed to the final status of Zr mineralization at Baerzhe. The hypersolvus granites
643 at Baerzhe, unlike the transsolvus rocks, were not affected by this invasive REE-Nb-Be-rich
644 fluid, as there is no visible hematization seen in these rocks. Given that the hypersolvus and
645 transsolvus granites have similar mineralogy, this is most likely related to lower porosity and
646 permeability of the hypersolvus rocks, likely related to the lack of autometasomatism and
647 alteration that would have developed porosity in the transsolvus rocks.
648

This is the peer-reviewed, final accepted version for American Mineralogist, published by the Mineralogical Society of America.
The published version is subject to change. Cite as Authors (Year) Title. American Mineralogist, in press.
DOI: https://doi.org/10.2138/am-2022-8336. http://www.minsocam.org/

649 The 124.86 ± 0.63 Ma U-Pb age of deuteric zircon (i.e., timing of Zr mineralization) and the
650 122.82 ± 0.62 Ma U-Pb age of monazite (i.e., timing of REE mineralization) in the miaskitic
651 phase, provided by Qiu et al. (2019), suggest that REE mineralization postdated zircon formation
652 in the transsolvus miaskitic granite. This is consistent with the fact that REE mineralization
653 occurs as replacement of zircon in both the miaskitic and agpaitic rocks (Wu et al., 2021). The
654 different types of zircon from the agpaitic phase should also postdate deuteric zircon in the
655 miaskitic phase, as the agpaitic phase is more evolved than the miaskitic phase albeit in the same
656 magmatic lineage (Wu et al., 2021). This is in line with the U-Pb age of the zircon pseudomorphs
657 (123.5 ± 3.2 Ma) reported by Yang et al. (2013), although the error in this age makes this
658 uncertain. A schematic diagram illustrating the development of alteration and zircon formation
659 associated with autometasomatism in the transsolvus miaskitic and agpaitic granites, and the
660 hematization and Be-REE-Nb mineralization that affected both types of granite is shown in
661 Figure 13.
662

663 ## CONCLUSIONS AND IMPLICATIONS

664 Documentation of the textural and chemical characteristics of metasomatic zircon from the REE-
665 Nb-Be-Zr-mineralized agpaitic granite Baerzhe using microbeam techniques, combined with
666 assessment of published data on zircon for the deposit, suggest that metasomatic zircon in the
667 agpaitic granite at Baerzhe precipitated from at least two different fluids. The inclusion zircon
668 within snowball quartz crystallized from the incipient fluid stage and was related to Na
669 metasomatism. Zircon and aegirine inclusions of this stage inherited the chemistry of this early
670 fluid. Partitioning of REE between zircon and aegirine explains the generally HREE-enriched
671 REE chondrite-normalized patterns of the inclusion zircon that are comparable to those of typical

magmatic zircon in granitic settings. Amphibole-replacement zircon, on the other hand, precipitated from a later fluid that contained higher Be and REE concentrations, especially LREE, than the Na-metasomatizing fluid. The REE-Be-rich nature of this late-stage fluid likely indicates a genetic relationship with the late-stage REE-Nb-Be-mineralizing event that affected both the miaskitic and agpaitic granites. The pseudomorph and elpidite-replacement zircon crystals share the same origin. It is unclear how the fluid responsible for their formation relates to the other fluids, but the pseudomorphs formed as a result of reaction between the Na-metasomatizing fluid and elpidite protocrysts. Acquisition of trace-element chemistry of unaltered elpidite would better constrain this model.

Comparison of the zircon characteristics with published oxygen isotope data (Yang et al., 2013) suggests that during the formation of the zircon-quartz pseudomorphs, the system was open and was infiltrated by meteoric water. The differences between metasomatic zircon in the agpaitic and miaskitic granites indicates that deuteric zircon in the miaskitic granite precipitated from a fluid that was constrained to that phase. Similarly, the early Zr-forming fluid in the agpaitic phase was constrained to that granite, and did not affect the miaskitic granite. This suggests that during Zr mineralization, both the miaskitic and agpaitic phases experienced autometasomatism that was restricted to their parental granites and did not migrate. This explains the localization of Na-metasomatism, in particular aegirine alteration of amphibole, to the agpaitic phase. A more pervasive REE-Nb-Be-rich fluid affected both the miaskitic and agpaitic granites at a later stage, and crystallized the amphibole-replacement zircon through localized interaction with the agpaitic phase. The multi-stage metasomatic zircon-forming events seen at Baerzhe reveal a more complex history of zircon formation in alkaline complexes than previously thought (Yang et al.,

This is the peer-reviewed, final accepted version for American Mineralogist, published by the Mineralogical Society of America.
The published version is subject to change. Cite as Authors (Year) Title. American Mineralogist, in press.
DOI: https://doi.org/10.2138/am-2022-8336. http://www.minsocam.org/

2013, 2014, 2020; Qiu et al., 2019; Wu et al., 2021). Such complexity in the formation of metasomatic zircon could apply to similar alkaline settings that contain high Zr endowments.

ACKNOWLEDGEMENTS

The present study was funded by an NSERC (Canada) Discovery Grant to I.M. Samson and by National Natural Science Foundation of China (NSFC) grants to Dehui Zhang (41773030) and Kunfeng Qiu (91962106). Sharon Lackie, Marc Beauchamp, Huan Hu, Jean Claude Barrette, and Melissa Price are thanked for their help during lab work. We acknowledge the comments and suggestions of Anouk Borst and an anonymous reviewer that greatly improved the paper.

REFERENCES

Bea, F. (1996) Residence of REE, Y, Th and U in Granites and Crustal Protoliths; Implications for the Chemistry of Crustal Melts. Journal of Petrology, 37, 521–552.

Bell, E.A., Boehnke, P., Barboni, M., and Harrison, T.M. (2019) Tracking chemical alteration in magmatic zircon using rare earth element abundances. Chemical Geology, 510, 56–71.

Beus, A.A. (1966) Geochemistry of Beryllium: And Genetic Types of Beryllium Deposits. WH Freeman.

Černý, P. (2002) Mineralogy of beryllium in granitic pegmatites. Reviews in Mineralogy and Geochemistry, 50, 405–444.

Dostal, J., Kontak, D., Gerel, O., Gregory Shellnutt, J., and Fayek, M. (2015) Cretaceous ongonites (topaz-bearing albite-rich microleucogranites) from Ongon Khairkhan, central Mongolia: Products of extreme magmatic fractionation and pervasive metasomatic fluid-rock interaction. Lithos, 236–237, 173–189.

Feng, Y., and Samson, I.M. (2015) Replacement processes involving high field strength elements in the T zone, Thor Lake rare-metal deposit. The Canadian Mineralogist, 53, 31–60.

Goldstein, R.H., and Rossi, C. (2002) Recrystallization in Quartz Overgrowths. Journal of Sedimentary Research, 72, 432–440.

Gysi, A.P., and Williams-Jones, A.E. (2013) Hydrothermal mobilization of pegmatite-hosted REE and Zr at Strange Lake, Canada: A reaction path model: Geochimica et Cosmochimica Acta, 122, 324–352.

Hanchar, J.M., Finch, R.J., Hoskin, P.W.O., Watson, E.B., Cherniak, D.J., and Mariano, A.N. (2001) Rare earth elements in synthetic zircon: Part 1. Synthesis, and rare earth element and phosphorus doping. American Mineralogist, 86, 667–680.

Hoskin, P.W.O. (2005) Trace-element composition of hydrothermal zircon and the alteration of hadean zircon from the Jack Hills, Australia. Geochimica et Cosmochimica Acta, 69, 637–648.

Hoskin, P.W.O., and Schaltegger, U. (2003) The composition of zircon and igneous and metamorphic petrogenesis. Reviews in Mineralogy and Geochemistry, 53, 27–62.

Kalashnikov, A. O., Konopleva, N. G., Pakhomovsky, Ya. A., and Ivanyuk, G. Yu. (2016) Rare Earth Deposits of the Murmansk Region, Russia—A Review A. Economic Geology, 111, 1529–1559.

736 Kovalenko, V.I., Tsaryeva, G.M., Goreglyad, A.V., Yarmolyuk, V.V., Troitsky, V.A., Hervig,
737 R.L. and Farmer, G. (1995) The peralkaline granite-related Khaldzan-Buregtey rare metal
738 (Zr, Nb, REE) deposit, western Mongolia. Economic Geology, 90, 530–547.
739 Kynicky, J., Chakhmouradian, A.R., Xu, C., Krmicek, L. and Galiova, M., 2011, Distribution
740 and evolution of zirconium mineralization in peralkaline granites and associated pegmatites
741 of the Khan Bogd complex, southern Mongolia. The Canadian Mineralogist, 49, 947–965.
742 Kynicky, J., Smith, M.P., and Xu, C. (2012) Diversity of rare earth deposits: The key example of
743 China. Elements, 8, 361–367.
744 Linnen, R., Trueman, D. L., and Burt, R. (2014) Tantalum and niobium. In Gunn, G., Ed.,
745 Critical Metals Handbook, p. 361–384. John Wiley and Sons, Oxford, U.K.
746 Marks, M.A., and Markl, G. (2017) A global review on agpaitic rocks. Earth-Science Reviews,
747 173, 229–258.
748 McDonough W.F., and Sun S.S. (1995) The composition of the Earth. Chemical Geology, 120,
749 223–253.
750 Michaud, J.A.S., and Pichavant, M. (2020) Magmatic fractionation and the magmatic-
751 hydrothermal transition in rare metal granites: Evidence from Argemela (Central
752 Portugal). Geochimica et Cosmochimica Acta, 289, 130–157.
753 Möller, V., and Williams-Jones, A.E. (2017) Magmatic and hydrothermal controls on the
754 mineralogy of the basal zone, Nechalacho REE-Nb-Zr deposit, Canada. Economic Geology,
755 112, 1823–1856.
756 Morimoto, N., Fabrie, J., Ferguson, A.K., Ginzburg, I.V., Ross, M., Seifert, F.A., and Zussman,
757 J. (1988) Nomenclature of pyroxenes. Mineralogical Magazine, 52, 535–550.
758 Nasdala, L., Irmer, G., and Wolf, D. (1995) The degree of metamictization in zircon: a Raman
759 spectroscopic study. European Journal of Mineralogy, 7, 471–478.
760 Nasdala, L., Wenze, l.M., Vavra, G., Irmer, G., Wenzel, T. and Kober, B. (2001)
761 Metamictisation of natural zircon: accumulation versus thermal annealing of radioactivity-
762 induced damage. Contribution to Mineralogy and Petrology, 141, 125–144.
763 Okamoto, A. and Sekine, K. (2011) Textures of syntaxial quartz veins synthesized by
764 hydrothermal experiments. Journal of Structural Geology, 33, 1764–1775.

765 Paton, C., Hellstrom, J., Paul, B., Woodhead, J., and Hergt, J. (2011) Iolite: Freeware for the
766 visualisation and processing of mass spectrometric data. Journal of Analytical Atomic
767 Spectrometry, 26, 2508–2518.
768 Pettke, T., Audétat, A., Schaltegger, U., and Heinrich, C.A. (2005) Magmatic-to-hydrothermal
769 crystallization in the W–Sn mineralized Mole Granite (NSW, Australia) Part II: Evolving
770 zircon and thorite trace element chemistry. Chemical Geology, 220, 191–213.
771 Putnis, A. (2002). Mineral replacement reactions: From macroscopic observations to
772 microscopic mechanisms. Mineralogical Magazine, 66, 689–708.
773 Qiu, K.F., Yu, H.C., Wu, M.Q., Geng, J.Z., Ge, X.K., Gou, Z.Y., and Taylor, R.D. (2019)
774 Discrete Zr and REE mineralization of the Baerzhe rare-metal deposit, China. American
775 Mineralogist, 104, 1487–1502.
776 Resentini, A., Andò, S., Garzanti, E., Malusà, M.G., Pastore, G., Vermeesch, P., Chanvry, E.,
777 and Dall'Asta, M. (2020) Zircon as a provenance tracer: Coupling Raman spectroscopy and
778 UP-b geochronology in source-to-sink studies. Chemical Geology, 555, 119828.
779 Rubin, J.N., Henry, C.D., and Price, J.G. (1989) Hydrothermal zircons and zircon overgrowths,
780 Sierra Blanca Peaks, Texas. American Mineralogist, 74, 865–869.
781 Rubin, J.N., Henry, C.D., and Price, J.G. (1993) The mobility of zirconium and other
782 “immobile” elements during hydrothermal alteration. Chemical Geology, 110, 1–3.
783 Schaltegger, U., Pettke, T., Audétat, A., Reusser, E., and Heinrich, C.A. (2005) Magmatic-to-
784 hydrothermal crystallization in the W–Sn mineralized Mole Granite (NSW, Australia): Part I:
785 Crystallization of zircon and REE-phosphates over three million years—a geochemical and
786 U–Pb geochronological study. Chemical Geology, 220, 215–235.
787 Schaltegger, U. (2007) Hydrothermal Zircon. Elements, 3, 51–79.
788 Verplanck, P. L., Mariano, A. N., and Mariano, A. Jr. (2016) Rare Earth Element Ore Geology
789 of Carbonatites. Reviews in Economic Geology, 18, 5–32.
790 Wall, F. (2014) Rare earth elements. In Gunn, G., Ed., Critical Metals Handbook, p. 311–339.
791 John Wiley and Sons, Oxford, U.K.
792 Wu, M.Q, Tian, B.F., Zhang, D.H., Xu, G.Z., Xu, W.X., and Qiu, K.F. (2018) Zircon of the No.
793 782 deposit from the Great Xing’an Range in NE China: Implications for Nb-REE-Zr
794 mineralization during magmatic-hydrothermal evolution. Ore Geology Reviews, 102, 284–
795 299.

796 Wu M.Q., Samson, I.M., Qiu K.F., and Zhang, D.H. (2021) Concentration Mechanisms of REE-
797 Nb-Zr-Be Mineralization in the Baerzhe Deposit, NE China: Insights from Textural and
798 Chemical Features of Amphibole and Rare-metal Minerals. Economic Geology, 116, 651–
799 679.
800 Xie, Y.L., Hou, Z.Q., Goldfarb, R. J., Guo, X., and Wang, L. (2016) Rare Earth Element
801 Deposits in China. Reviews in Economic Geology, 18,115–136.
802 Yang W., Lin Y.T., Hao J.L., Zhang J.C., Hu S., and Ni H.W. (2016) Phosphorus-controlled
803 trace element distribution in zircon revealed by NanoSIMS. Contributions to Mineralogy and
804 Petrology, 171, 28.
805 Yang, W.B., Niu, H.C., Sun, W.D., Shan, Q., Zheng, Y.F., Li, N.B., Li, C.Y., Arndt, N.T., Xu,
806 X., Jiang, Y.H., and Yu, X.Y. (2013) Isotopic evidence for continental ice sheet in mid-
807 latitude region in the supergreenhouse Early Cretaceous. Scientific Reports, 3, 2732.
808 Yang, W.B., Niu, H.C., Shan, Q., Sun, W.D., Zhang, H., Li, N.B., Jiang,Y.H., and Yu, X.Y.
809 (2014) Geochemistry of magmatic and hydrothermal zircon from the highly evolved Baerzhe
810 alkaline granite: implications for Zr–REE–Nb mineralization. Mineralium Deposita, 49, 451–
811 470.
812 Yang, W.B., Niu, H.C., Li, N.B., Hollings, P., Zurevinski, S., and Xing, C.M. (2020) Enrichment
813 of REE and HFSE during the magmatic-hydrothermal evolution of the Baerzhe alkaline
814 granite, NE China: Implications for rare metal mineralization. Lithos, 358–359, 105–411.
815 Zhang, M., Salje, E.K., Farnan, I., Graeme-Barber, A., Daniel, P., Ewing, R.C., Clark, A.M. and
816 Leroux, H. (2000) Metamictization of zircon: Raman spectroscopic study. Journal of
817 Physics: Condensed Matter, 12, 1915.

This is the peer-reviewed, final accepted version for American Mineralogist, published by the Mineralogical Society of America.
The published version is subject to change. Cite as Authors (Year) Title. American Mineralogist, in press.
DOI: https://doi.org/10.2138/am-2022-8336. http://www.minsocam.org/

Fig. 1

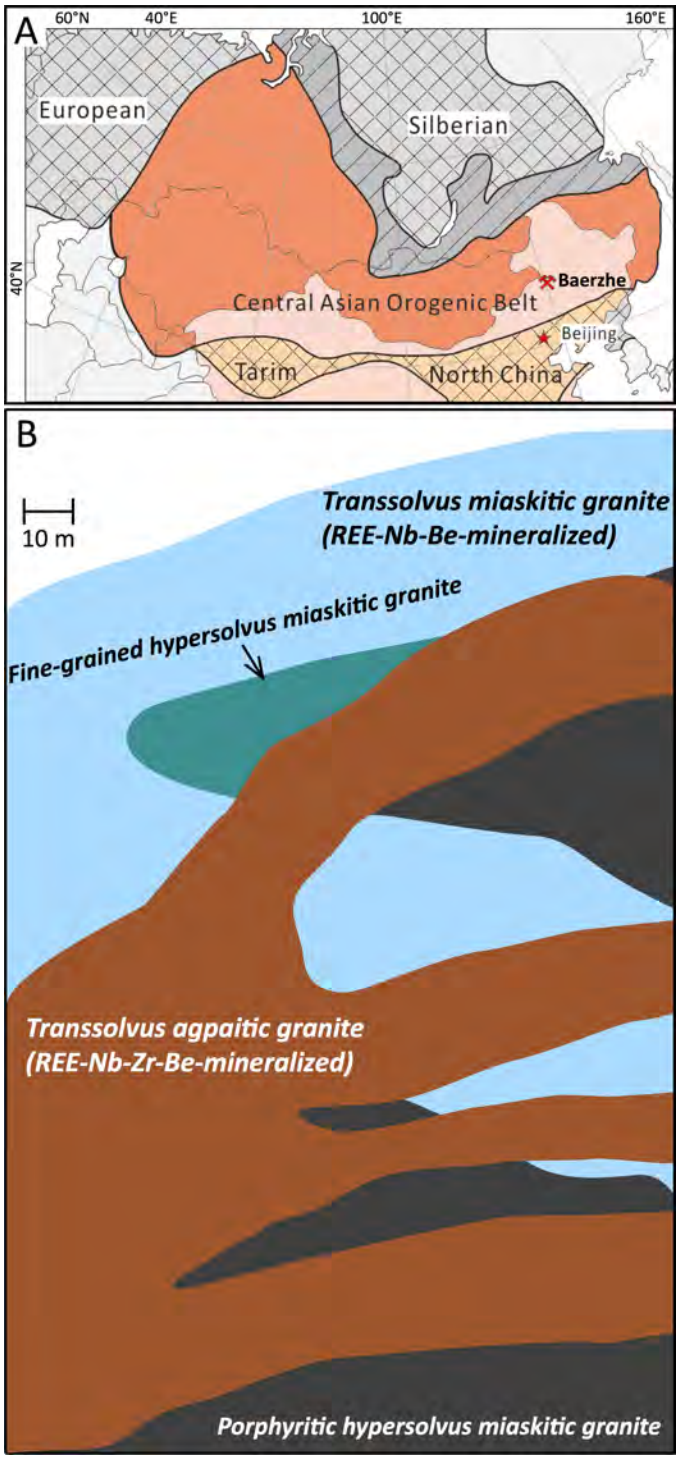

Figure 1. (A) Location of the Baerzhe deposit in China, at the eastern part of Central Asian orogenic belt. (B) A sketch that shows the distribution and relationships of the four rock types identified by Wu et al. (2021) at the Baerzhe granitic complex. The two transsolvus granites are mineralized, whereas the two hypersolvus granites are unmineralized.

This is the peer-reviewed, final accepted version for American Mineralogist, published by the Mineralogical Society of America.
The published version is subject to change. Cite as Authors (Year) Title. American Mineralogist, in press.
DOI: https://doi.org/10.2138/am-2022-8336. http://www.minsocam.org/

Fig. 2

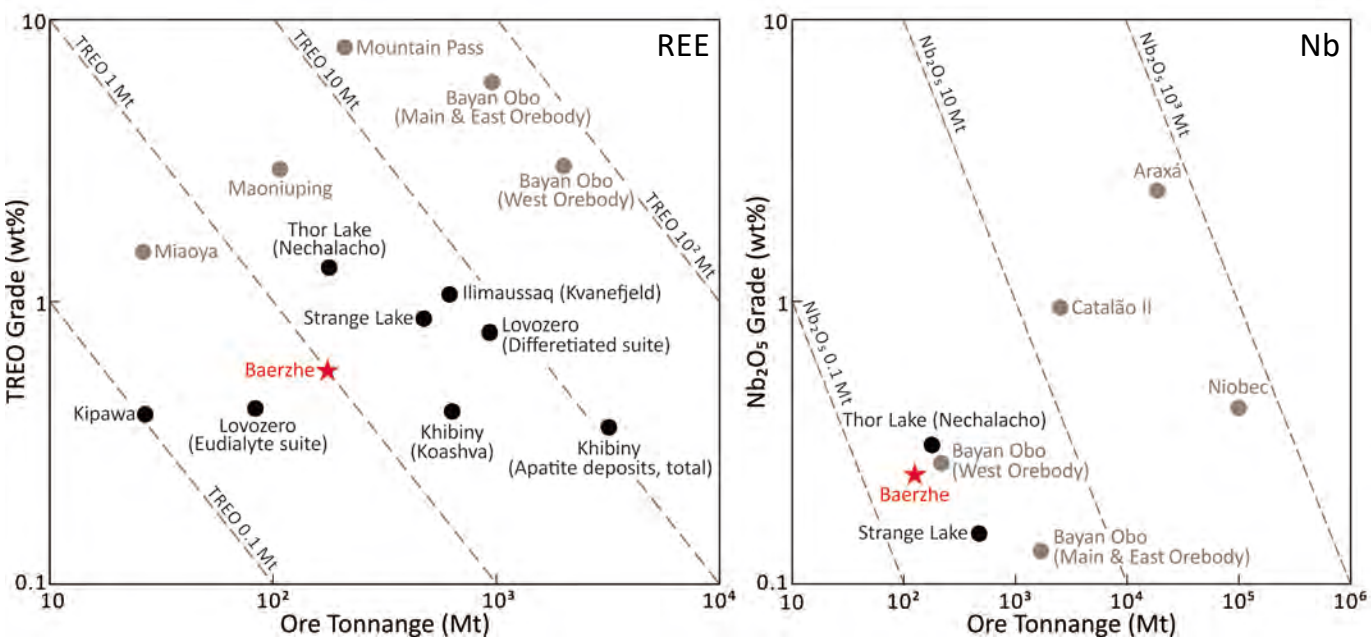

Figure 2. Ore grade vs. tonnage diagrams for REE and Nb mineralization that show how Baerzhe compares to other important deposits (black solid circles: mineralization in alkaline-peralkaline settings; grey solid circles: mineralization in carbonatites). Data after Wall (2014), Linnen et al. (2014), Dostal (2016), Kalashnikov et al. (2016), Verplanck et al. (2016), Xie et al. (2016), and Wu et al. (2021).

This is the peer-reviewed, final accepted version for American Mineralogist, published by the Mineralogical Society of America.
The published version is subject to change. Cite as Authors (Year) Title. American Mineralogist, in press.
DOI: https://doi.org/10.2138/am-2022-8336. http://www.minsocam.org/

Fig. 3

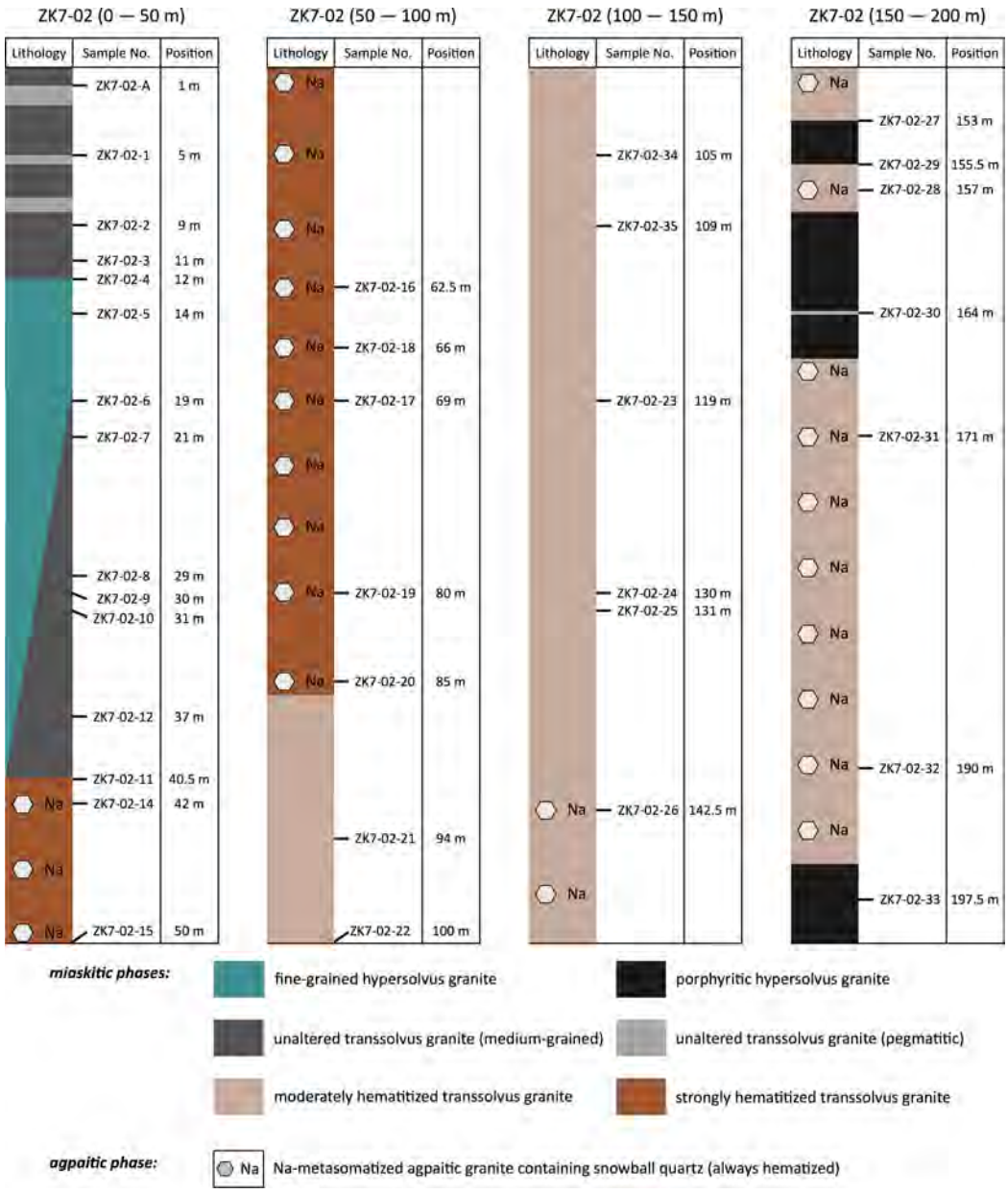

Figure 3. Rock types in the ZK7-02 drill core from 0 to 200 m, showing sampling locations and distribution of Na metasomatism, hematization, and snowball quartz. Note that Na metasomatism and snowball quartz are both restricted to the hematized transolvus granite.

This is the peer-reviewed, final accepted version for American Mineralogist, published by the Mineralogical Society of America.
The published version is subject to change. Cite as Authors (Year) Title. American Mineralogist, in press.
DOI: https://doi.org/10.2138/am-2022-8336. http://www.minsocam.org/

Fig. 4

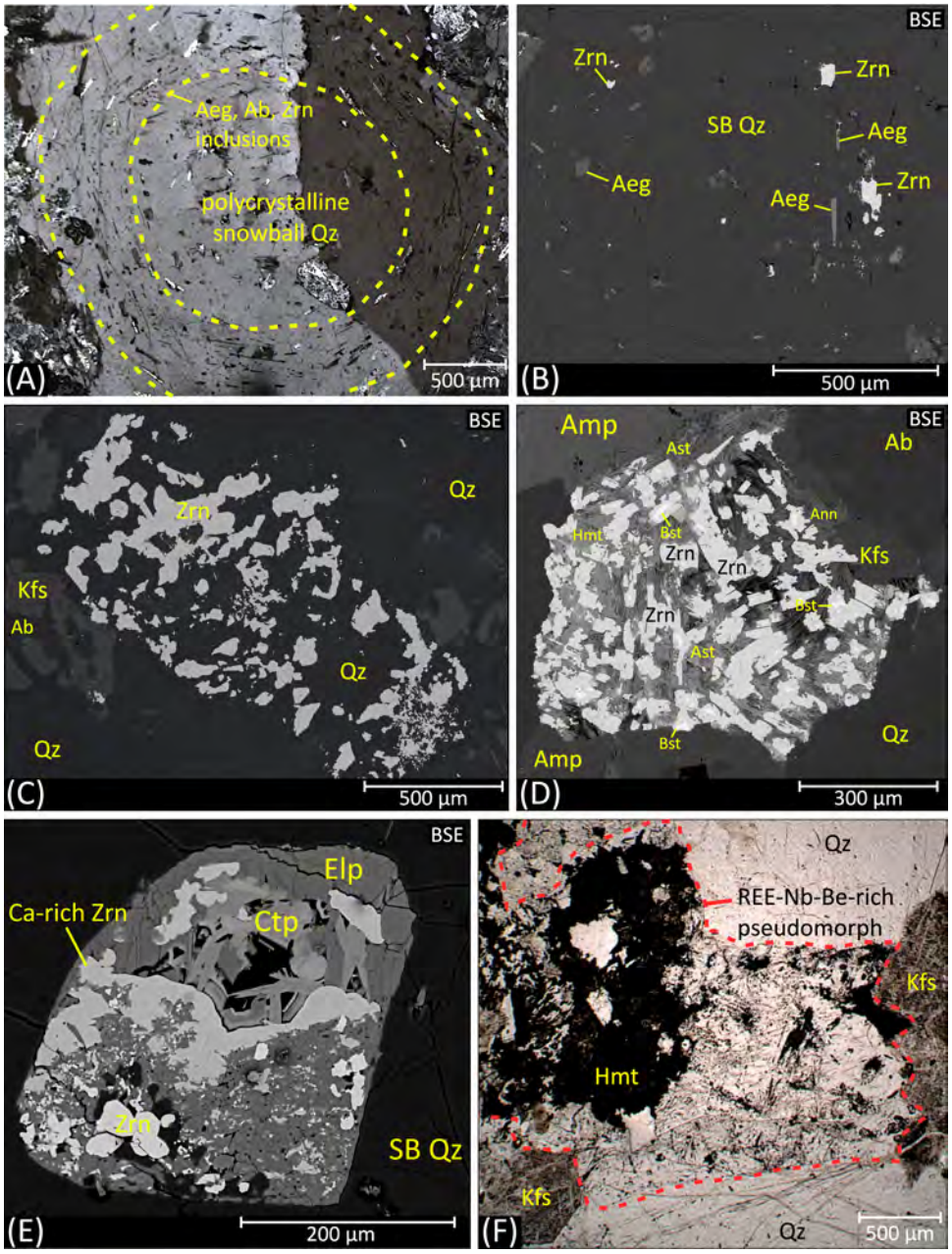

Figure 4. Optical and back-scattered (BSE) photomicrographs of representative textures and types of metasomatic zircon in the agpaitic granite at Baerzhe: (A) A polycrystalline snowball quartz aggregate that contains aegirine, albite, and zircon inclusions with a concentric arrangement. The yellow dashed lines delineate the concentric zoning of inclusion minerals. (B) Aegirine and zircon inclusions in a snowball quartz crystal. (C) Pseudomorph zircon, which occurs in a large, euhedral pseudomorph that contains subequal amounts of zircon and quartz. (D) Amphibole-replacement zircon that occurs in association with astrophyllite, hematite, and annite, formed through partial replacement of amphibole (cf. Wu et al., 2021). This type of zircon was partially replaced by bastnäsite. (E) A snowball quartz-hosted elpidite crystal that has been partially replaced by calciocatapleiite, and the elpidite-replacement zircon (cf. Wu et al., 2021). (F) A REE-Nb-Be-rich pseudomorph, mainly comprising hingganite, aeschynite, and hematite, hosted by a secondary quartz aggregate. Abbreviations: Ab = albite, Aeg = aegirine, Amp = amphibole, Ann = annite; Ast = astrophyllite, Bst = bastnäsite; Ctp = calciocatapleiite, Elp = elpidite, Hmt = hematite, Kfs = K-feldspar, Qz = quartz, SB = snowball, Zrn = zircon

This is the peer-reviewed, final accepted version for American Mineralogist, published by the Mineralogical Society of America.
The published version is subject to change. Cite as Authors (Year) Title. American Mineralogist, in press.
DOI: https://doi.org/10.2138/am-2022-8336. http://www.minsocam.org/

Fig. 5

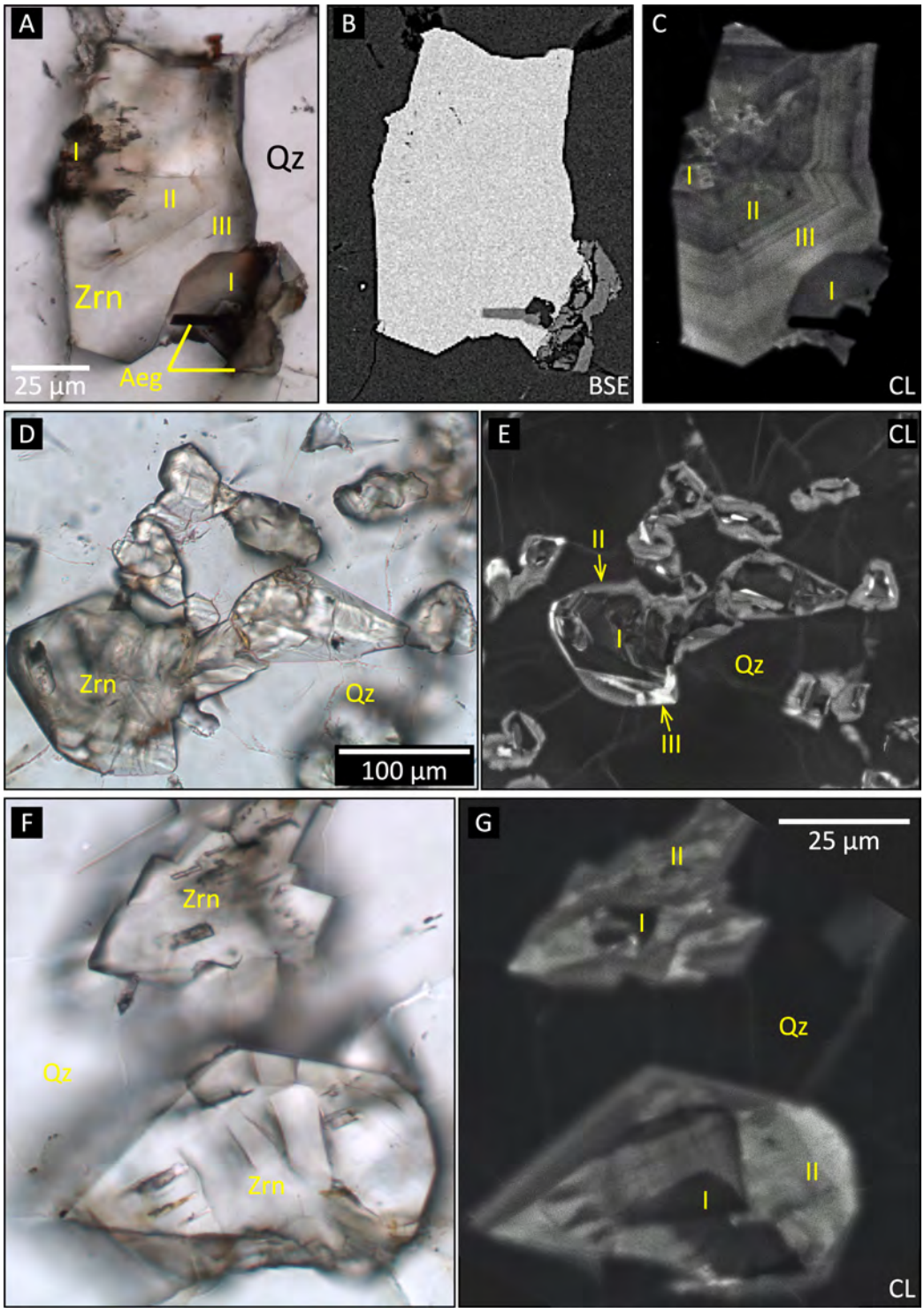

Figure 5. Representative optical, BSE, and cathodoluminescence (CL) photomicrographs of the inclusion and pseudomorph zircon: (A – C) Optical, BSE, and CL images of an inclusion zircon crystal. I, II, and III refer to the different domains of the inclusion zircon crystal (see text for details). (D and E) Optical and CL images of pseudomorph zircon crystals. (F – G) Optical and CL images of two pseudomorph zircon crystals. I, II, and III refer to the different domains of the pseudomorph zircon crystal (see text for details).

This is the peer-reviewed, final accepted version for American Mineralogist, published by the Mineralogical Society of America.
The published version is subject to change. Cite as Authors (Year) Title. American Mineralogist, in press.
DOI: https://doi.org/10.2138/am-2022-8336. http://www.minsocam.org/

Fig. 6

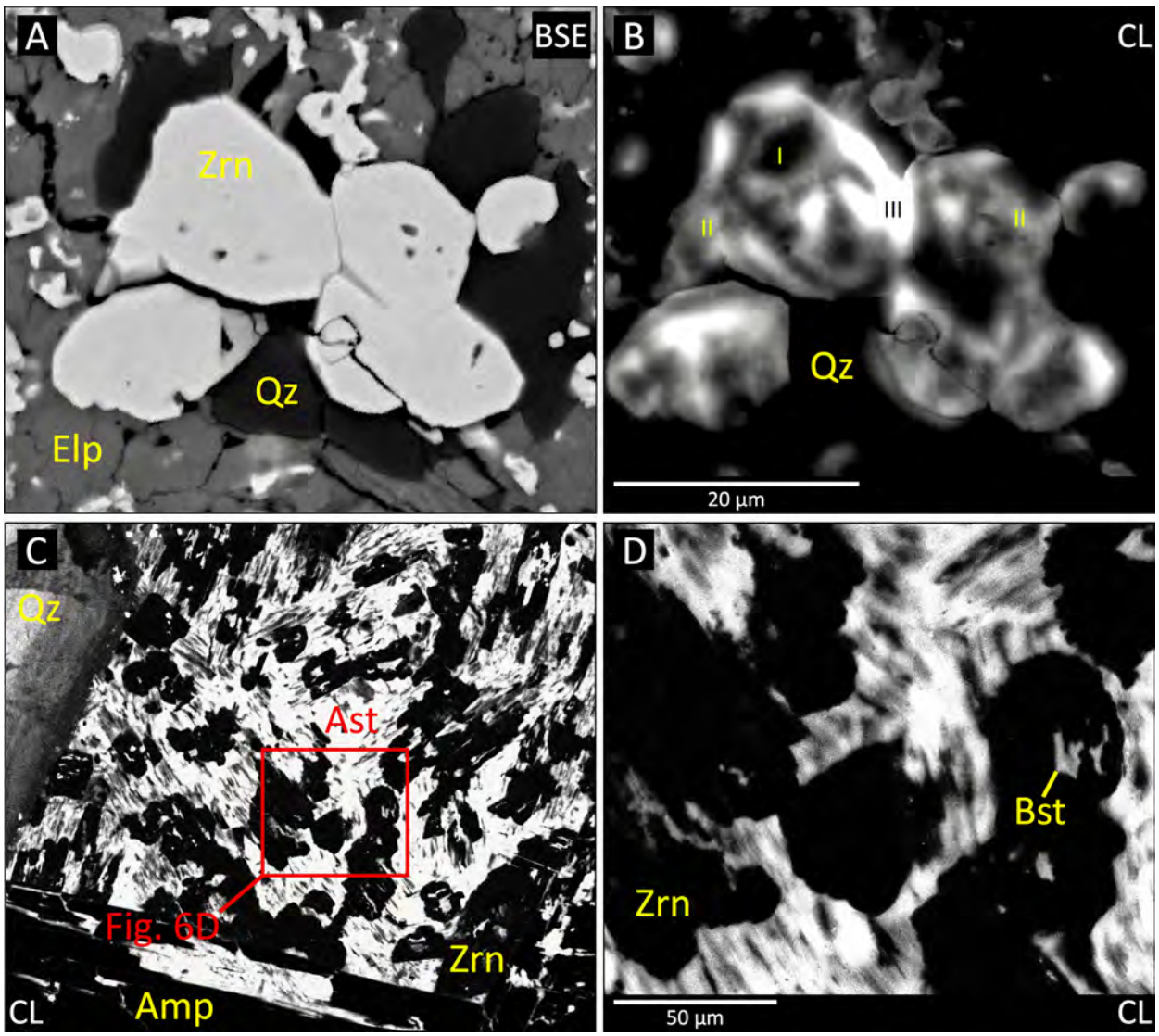

Figure 6. Representative BSE and CL photomicrographs of the elpidite-replacement and amphibole-replacement zircon: (A and B) BSE and CL images of elpidite-replacement zircon crystals. (C and D) CL images of amphibole-replacement zircon crystals.

This is the peer-reviewed, final accepted version for American Mineralogist, published by the Mineralogical Society of America.
The published version is subject to change. Cite as Authors (Year) Title. American Mineralogist, in press.
DOI: https://doi.org/10.2138/am-2022-8336. http://www.minsocam.org/

Fig. 7

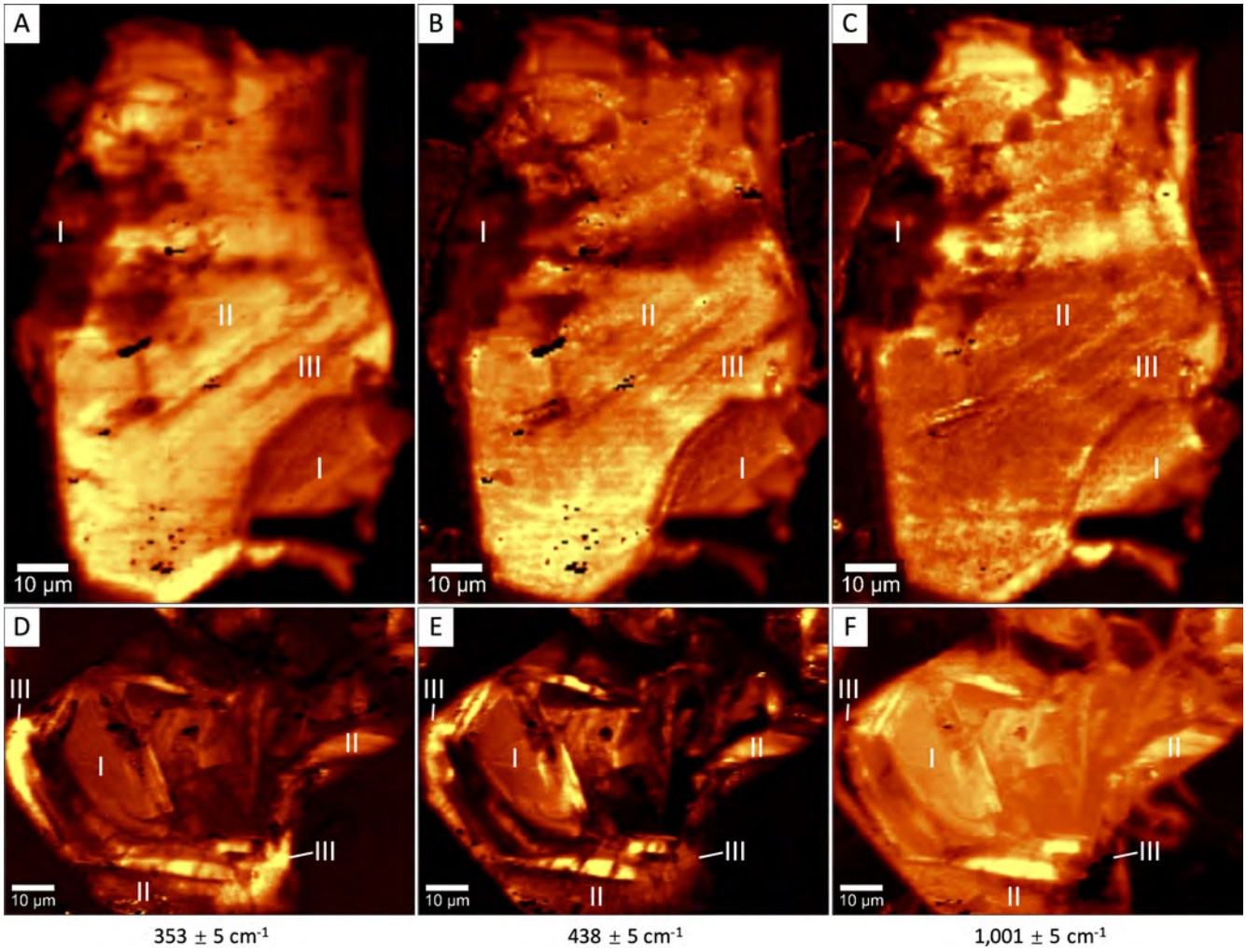

Figure 7. (A, B, and C) Automated Raman filter maps for an inclusion zircon crystal, tuned respectively, to the 353 ± 5 cm^{-1}, 438 ± 5 cm^{-1}, and 1,001 ± 5 cm^{-1} bands. (D, E, and F) Automated Raman filter maps of a pseudomorph zircon crystal, tuned respectively, to the 353 ± 5 cm^{-1}, 438 ± 5 cm^{-1}, and 1,001 ± 5 cm^{-1} bands. I, II, and III refer to the different domains of an individual zircon crystal (see text for details).

This is the peer-reviewed, final accepted version for American Mineralogist, published by the Mineralogical Society of America.
The published version is subject to change. Cite as Authors (Year) Title. American Mineralogist, in press.
DOI: https://doi.org/10.2138/am-2022-8336. http://www.minsocam.org/

Fig. 8

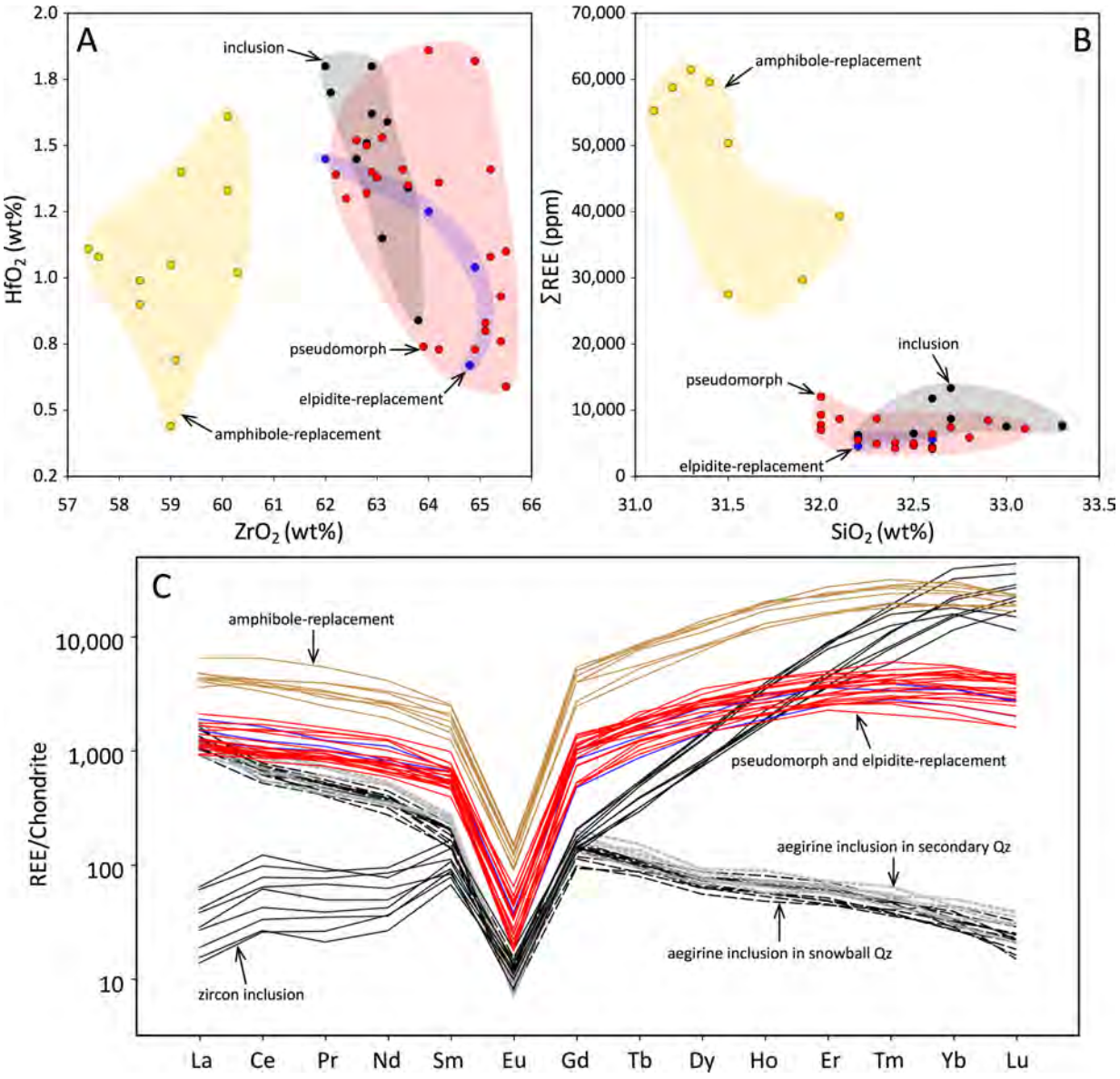

Figure 8. Bivariate plots of (A) HfO_2 vs. ZrO_2 concentrations and (B) ΣREE vs. SiO_2 concentrations in the various types of zircon at Baerzhe. (C) Chondrite-normalized spider diagram of the different types of zircon and aegirine inclusions from the agpaitic granite at Baerzhe. Chondrite values after McDonough and Sun (1995).

This is the peer-reviewed, final accepted version for American Mineralogist, published by the Mineralogical Society of America.
The published version is subject to change. Cite as Authors (Year) Title. American Mineralogist, in press.
DOI: https://doi.org/10.2138/am-2022-8336. http://www.minsocam.org/

Fig. 9

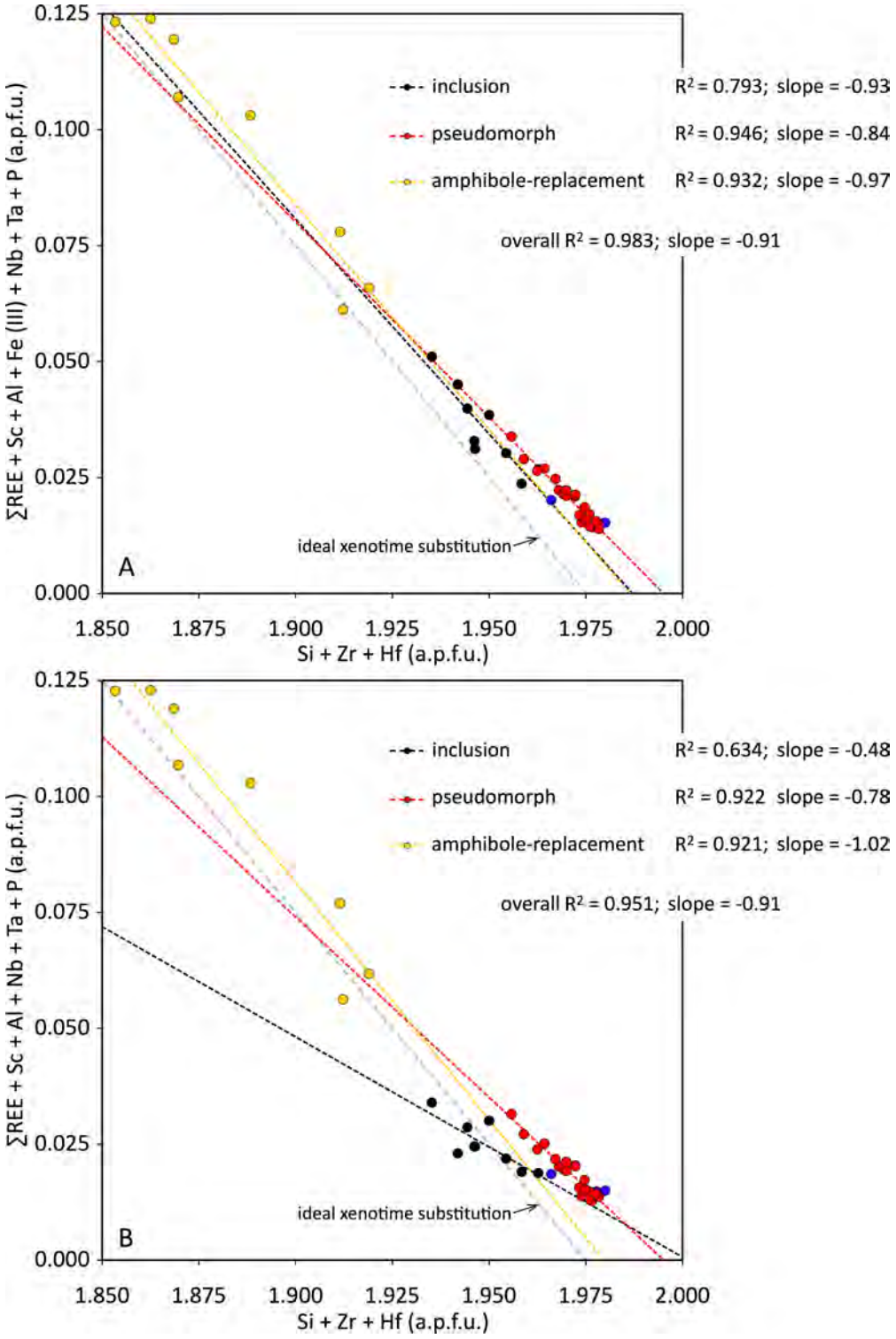

Figure 9. (A) The a.p.f.u. sum of trivalent and pentavalent cations (ΣREE + Sc + Al + Fe^{3+} + Nb + Ta + P) vs. the a.p.f.u. sum of the tetravalent cations (Si + Zr + Hf) of the different types of metasomatic zircon. (B) The same plot as (A) but excluding Fe, i.e., if Fe is present as Fe^{2+}. The negative correlation with a slope close to -1 shows that the examined zircon displays a xenotime substitution, the dominant crystal-chemical control for trace-element accommodation in zircon.

This is the peer-reviewed, final accepted version for American Mineralogist, published by the Mineralogical Society of America.
The published version is subject to change. Cite as Authors (Year) Title. American Mineralogist, in press.
DOI: https://doi.org/10.2138/am-2022-8336. http://www.minsocam.org/

Fig. 10

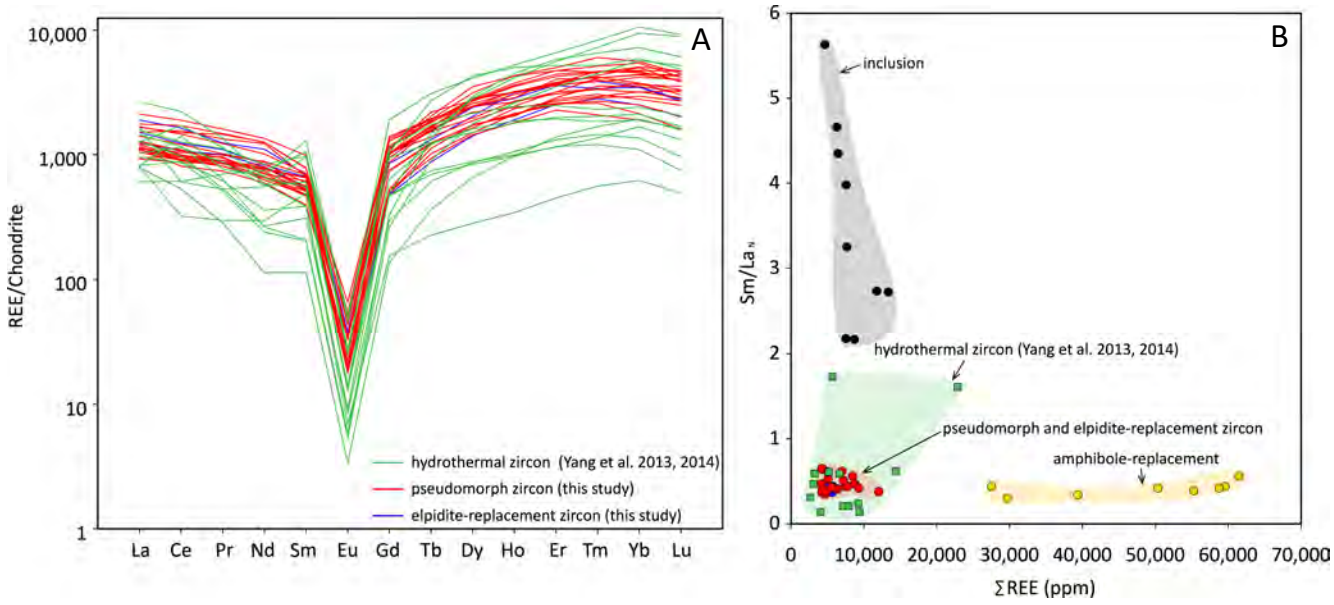

Figure 10. A comparison of the REE chemistry of the hydrothermal zircon reported by Yang et al. (2013, 2014) to the pseudomorph and elpidite-replacement zircon examined in this study. (A) Chondrite-normalized plot of the three types. (B) A Sm/La_N vs. ΣREE plot of the three types together with the inclusion and amphibole-replacement zircon. The three types of zircon are comparable and are distinct from the inclusion and amphibole-replacment zircon.

This is the peer-reviewed, final accepted version for American Mineralogist, published by the Mineralogical Society of America.
The published version is subject to change. Cite as Authors (Year) Title. American Mineralogist, in press.
DOI: https://doi.org/10.2138/am-2022-8336. http://www.minsocam.org/

Fig. 11

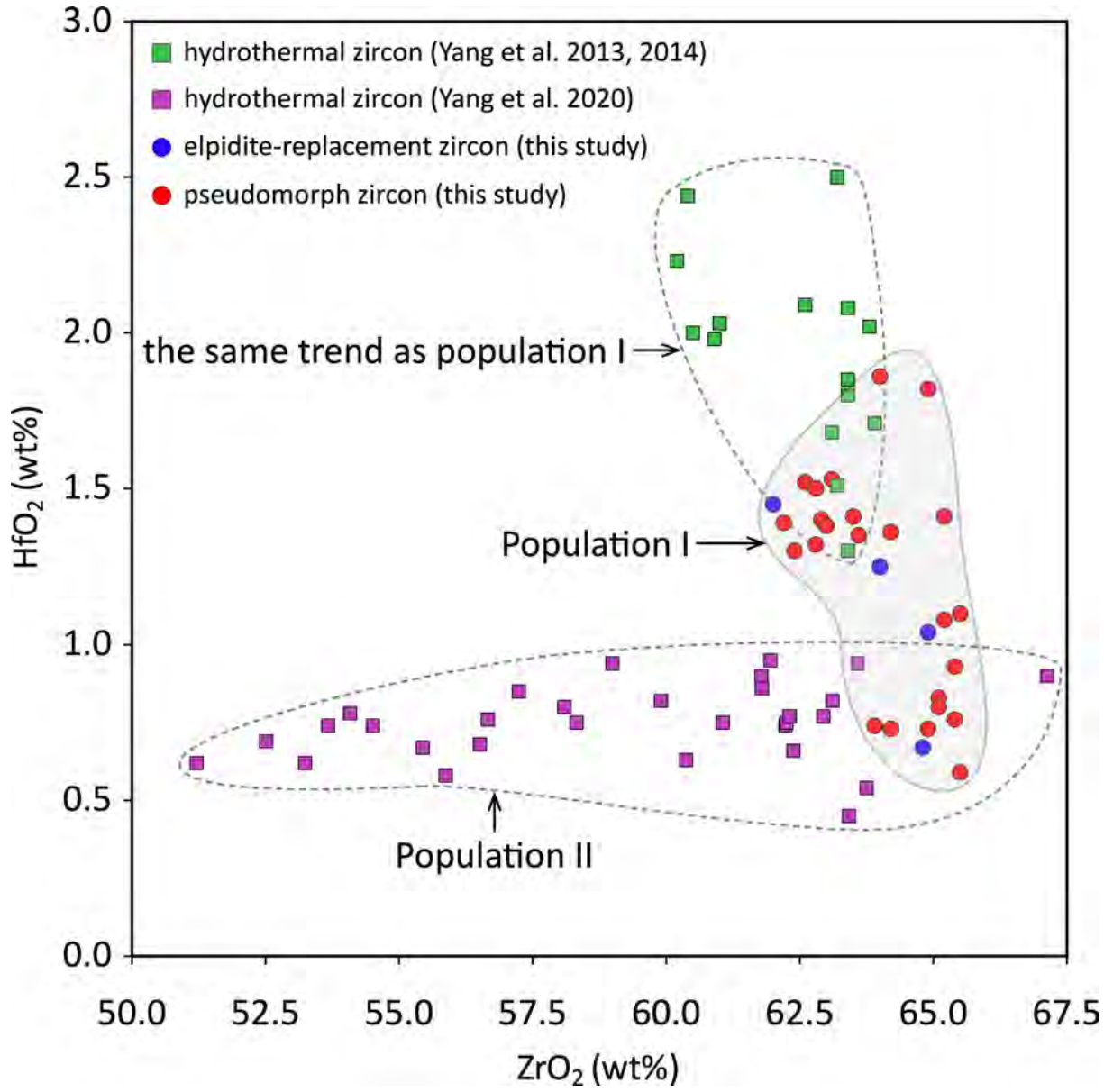

Figure 11. Comparison of the pseudomorph and elpidite-replacement zircon reported in this study with the hydrothermal zircon reported by Yang et al. (2013, 2014, 2020), on a bivariate plot of HfO_2 vs. ZrO_2 concentrations. This plot demonstrates that there are two populations of zircon: Population I comprises the pseudomorph/elpidite-replacement zircon and the hydrothermal zircon reported by Yang et al. (2013, 2014), and Population II comprises the hydrothermal zircon reported by Yang et al. (2020).

This is the peer-reviewed, final accepted version for American Mineralogist, published by the Mineralogical Society of America.
The published version is subject to change. Cite as Authors (Year) Title. American Mineralogist, in press.
DOI: https://doi.org/10.2138/am-2022-8336. http://www.minsocam.org/

Fig. 12

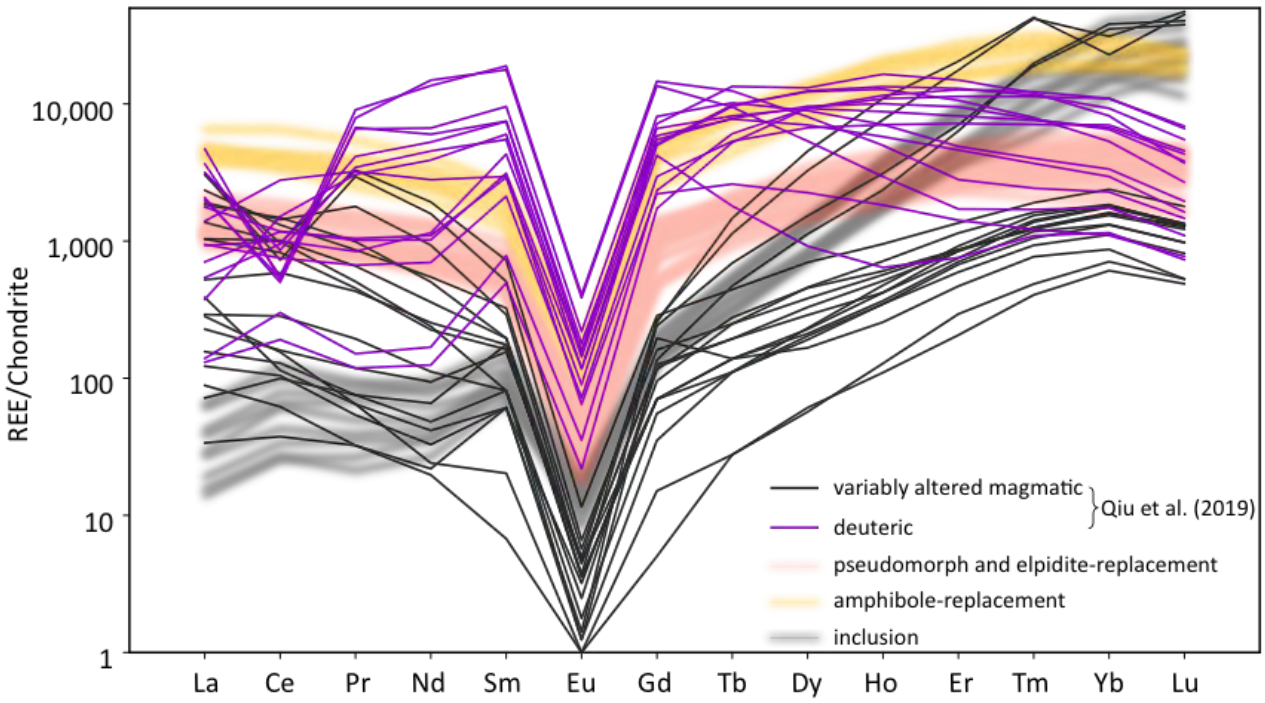

Figure 12. Chondrite-normalized REE distributions of the altered and deuteric zircon in the altered miaskitic granite reported by Qiu et al. (2019) and the metasomatic zircon in the agpaitic granite. This plot shows that the chemistry of metasomatic zircon from the agpaitic granite is different to the altered or deuteric zircon in the miaskitic phase.

This is the peer-reviewed, final accepted version for American Mineralogist, published by the Mineralogical Society of America.
The published version is subject to change. Cite as Authors (Year) Title. American Mineralogist, in press.
DOI: https://doi.org/10.2138/am-2022-8336. http://www.minsocam.org/

Fig. 13

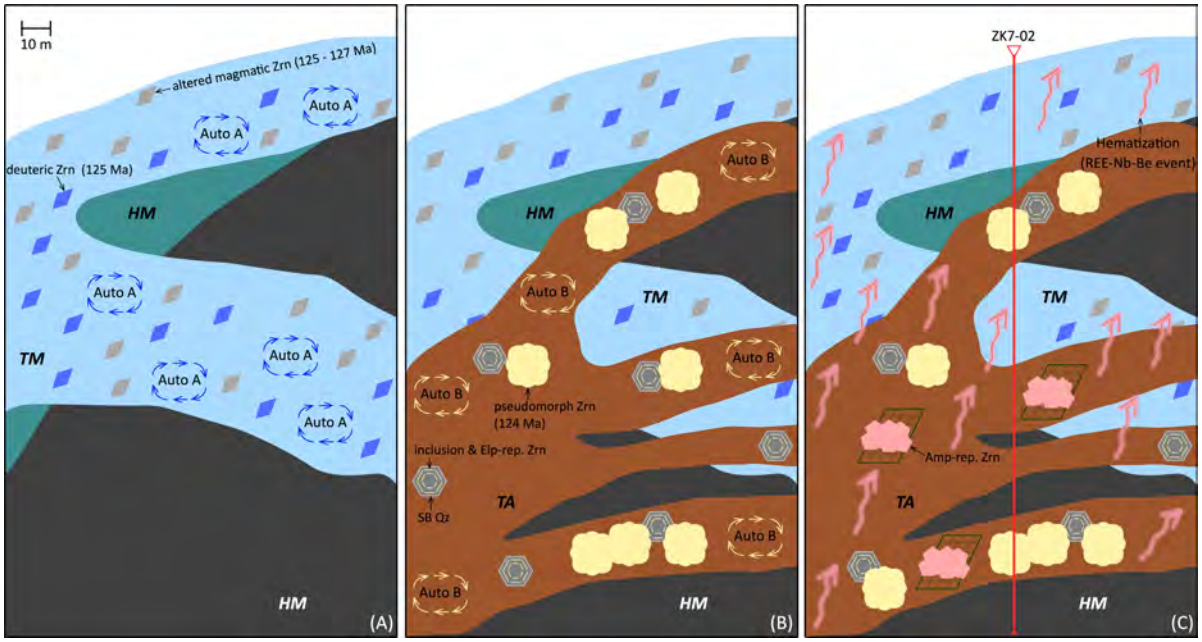

Figure 13. A schematic diagram illustrating the emplacement sequences (A - C), autometasomatism, and hematization (REE-Nb-Be-mineralizing event) of the Baerzhe miaskitic-agpaitic complex, and their impact on multi-stage metasomatic zircon crystallization. Abbreviations: HM = hypersolvus miaskitic granites, namely the fine-grained and porphyritic hypersolvus phases; TM = transsolvus miaskitic granite; TA = transsolvus agpaitic granite; Auto A = autometasomatism in the transsolvus miaskitic granite; Auto B = autometasomatism in the transsolvus agpaitic granite.

Table 1. Compilation of rock and zircon types described at Baerzhe in some recent literatures

Rock type	Type of samples described	References	Agpaitic/miaskitic	Mineralization	Alteration	Zircon occurrence	Zircon origin	Comments
Fine-grained/porphyritic hypersolvus granite	Core and surface rock samples	Wu et al. (2021)	Miaskitic	None	Unaltered	In equilibrium with amphibole and perthite	Magmatic	
Unaltered transsolvus granite	Core and surface rock samples	Wu et al. (2021)	Miaskitic	None	Unaltered	In equilibrium with amphibole and perthite	Magmatic	
Hematized transsolvus granite	Core and surface rock samples	Qiu et al. (2019), Wu et al. (2021), this study	Miaskitic	REE-Nb-Be	Hematization	In equilibrium with amphibole, perthite, and quartz (altered magmatic zircon); enclosed in quartz as aggregates (deuteric zircon)	Altered magmatic and deuteric	Originally described by Qiu et al. (2019) as the mineralized transsolvus granite
Na-metasomatized transsolvus granite	Core and surface rock samples	Wu et al. (2021), this study	Agpaitic	Zr + REE-Nb-Be	Na metasomatism	Inclusion in snowball quartz; pseudomorph after primary zirconosilicate minerals; partial replacement of elpidite; partial replacement of amphibole	Metasomatic	
Hypersolvus granite	Zircon mineral separates	Yang et al. (2013, 2014)	N.A.	None	N.A.	N.A.	Magmatic	
Subsolvus granite	Zircon mineral separates	Yang et al. (2013, 2014)	N.A.	Zr + REE-Nb-Be	N.A.	N.A.	Hydrothermal	Whether this is the same phase investigated later by Yang et al. (2020) is unknown
Subsolvus granite	Core and surface rock samples	Yang et al. (2020)	N.A.	Zr + REE-Nb-Be	Na metasomatism	Mineral clusters in quartz	Hydrothermal	The transsovlus nature of this granite was misinterpreted as subsolvus; hydrothermal zircon is analogous to the pseudomorph type described in Wu et al. (2017) and this study

Abbreviations: N.A. = not available